

# Probing the evolutionary status of starless cores through $\text{N}_2\text{H}^+$ and $\text{N}_2\text{D}^+$ observations

A. Crapsi<sup>1,2</sup>, P. Caselli<sup>3</sup>, C.M. Walmsley<sup>3</sup>, P.C. Myers<sup>2</sup>, M. Tafalla<sup>4</sup>, C.W. Lee<sup>5</sup>, T.L. Bourke<sup>6</sup>

## ABSTRACT

We have undertaken a survey of  $\text{N}_2\text{H}^+$  and  $\text{N}_2\text{D}^+$  towards 31 low-mass starless cores using the IRAM 30-m telescope. Our main objective has been to determine the abundance ratio of  $\text{N}_2\text{D}^+$  and  $\text{N}_2\text{H}^+$  towards the nuclei of these cores and thus to obtain estimates of the degree of deuterium enrichment, a symptom of advanced chemical evolution according to current models. We find that the  $\text{N}(\text{N}_2\text{D}^+)/\text{N}(\text{N}_2\text{H}^+)$  ratio is larger in more “centrally concentrated cores” with larger peak  $\text{H}_2$  and  $\text{N}_2\text{H}^+$  column density than the sample mean. The deuterium enrichment in starless cores is presently ascribed to depletion of CO in the high density ( $> 3 \times 10^4 \text{ cm}^{-3}$ ) core nucleus. To substantiate this picture, we compare our results with observations in dust emission at 1.2 mm and in two transitions of  $\text{C}^{18}\text{O}$ . We find a good correlation between deuterium fractionation and  $\text{N}(\text{C}^{18}\text{O})/\text{N}(\text{H}_2)_{1.2 \text{ mm}}$  for the nuclei of 14 starless cores. We, thus, identified a set of properties that characterize the most evolved, or “pre–stellar”, starless cores. These are: higher  $\text{N}_2\text{H}^+$  and  $\text{N}_2\text{D}^+$  column densities, higher  $\text{N}(\text{N}_2\text{D}^+)/\text{N}(\text{N}_2\text{H}^+)$ , more pronounced CO depletion, broader  $\text{N}_2\text{H}^+$  lines with infall asymmetry, higher central  $\text{H}_2$  column densities and a more compact density profile than in the average core. We conclude that this combination of properties gives a reliable indication of the evolutionary state of the core. Seven cores in our sample (L1521F, OphD, L429, L694, L183, L1544 and TMC2) show the majority of these features

---

<sup>1</sup>Università degli Studi di Firenze, Dipartimento di Astronomia e Scienza dello Spazio, Largo E. Fermi 5, I-50125 Firenze, Italy

<sup>2</sup>Harvard–Smithsonian Center for Astrophysics, 60 Garden Street, Cambridge, MA 02138, USA

<sup>3</sup>INAF–Osservatorio Astrofisico di Arcetri, Largo E. Fermi 5, I-50125 Firenze, Italy

<sup>4</sup>Observatorio Astronómico Nacional (IGN), Alfonso XII, 3, E-28014 Madrid, Spain

<sup>5</sup>Korea Astronomy Observatory, 61-1 Hwaam-dong, Yusung-gu, Daejon 305-348, Korea

<sup>6</sup>Harvard–Smithsonian Center for Astrophysics, Submillimeter Array Project, 645 N. A’ohoku Place, Hilo, HI 96720, USA

and thus are believed to be closer to forming a protostar than are the other members of our sample. Finally, we note that the subsample of Taurus cores behaves more homogeneously than the total sample, an indication that the external environment could play an important role in the core evolution.

*Subject headings:* ISM: clouds – ISM: evolution – ISM: kinematics and dynamics – ISM: molecules – stars: formation

## 1. Introduction

Understanding the physical and kinematic conditions in a molecular cloud core just prior to the onset of gravitational collapse is of paramount importance if one wishes to study the subsequent protostellar evolution. Molecular line measurements can provide the kinematical informations to probe infall motions in the highest density nucleus as long as the observed species is reasonably abundant in the region of interest.

An important step forward in the starless core studies has been the understanding of the fact that, at temperatures of roughly 10 K and densities above a few times  $10^4 \text{ cm}^{-3}$ , CO, as well as other carbon-bearing molecules, condenses out onto dust grain surfaces preventing us from observing the high density structures from where one expects the first signs of collapse (Leger 1983). This is most clearly seen from the comparison of maps made in the millimeter dust continuum with maps of CO isotopomers (Kuiper et al. 1996; Kramer et al 1999; Alves et al. 1999; Caselli et al. 1999).

For reasons which are thought to have to do with the low binding energy of the  $\text{N}_2$  molecule on ice mantle surfaces (Sadlej et al. 1995; Bergin & Langer 1997), there are some N-containing molecular species which survive in the gas phase at least for densities in the range  $10^5$  to  $10^6 \text{ cm}^{-3}$ . In particular, maps of  $\text{N}_2\text{H}^+$  and  $\text{NH}_3$  (as well as their deuterated counterparts) show reasonable agreement with the distribution of dust emission. Thus, only from observations of such species one can hope to probe the physical and chemical conditions of the most evolved pre-stellar cores which show a high column density peak in the dust emission.

One can also hope that by studying samples of such high density objects it will be possible to identify the cores where collapse has already been initiated or is at the point of doing so.

The aim of the current article is to report the results of a survey of 31 cores in various transitions of  $\text{N}_2\text{H}^+$  and  $\text{N}_2\text{D}^+$  observed with the IRAM 30-m telescope.

These observations, besides probing the kinematics of the high density nucleus of starless cores, enable us to gauge the deuterium enrichment in our sample. This parameter, evaluated

from the  $\text{N}_2\text{D}^+$  over  $\text{N}_2\text{H}^+$  column density ratio, can be used as a tool to discriminate the evolutionary status of a starless core. In fact, the disappearance of CO from the gas phase, together with the exothermicity of the production of  $\text{H}_2\text{D}^+$ , leads to abundances of deuterated species in cold molecular clouds more than 3 orders of magnitudes larger than the  $[\text{D}]/[\text{H}]$  elemental abundance ( $\simeq 1.5 \times 10^{-5}$  Oliveira et al. 2003). The freeze-out of the CO onto the grain mantles decreases the destruction of  $\text{H}_2\text{D}^+$  and  $\text{H}_3^+$ . As a result, the enhanced  $\text{H}_3^+$  abundance speeds up the reaction that leads to a higher production of  $\text{H}_2\text{D}^+$  and this increases the ratio of  $[\text{H}_2\text{D}^+]/[\text{H}_3^+]$  (e.g. Dalgarno & Lepp 1984; Roberts & Millar 2000).

We expect to use the  $\text{N}(\text{N}_2\text{D}^+)/\text{N}(\text{N}_2\text{H}^+)$  ratio to discriminate the less evolved starless cores from the more advanced pre–stellar cores. For practical purposes in this study, we define “pre–stellar cores” to be those with an  $\text{N}(\text{N}_2\text{D}^+)/\text{N}(\text{N}_2\text{H}^+)$  abundance ratio  $\geq 0.1$  and we believe that this approximately corresponds to a core with central density greater than  $5 \times 10^5 \text{ cm}^{-3}$  which are in the last phase of their evolution prior to dynamical collapse. We base this partly on the cross-correlation of our  $\text{N}(\text{N}_2\text{D}^+)/\text{N}(\text{N}_2\text{H}^+)$  measurements with other properties expected to probe an enhanced evolution of the starless cores such as broader line widths, larger  $n(\text{H}_2)$  central density or bigger amount of CO freeze-out. For this reason, supplemental dust continuum and  $\text{C}^{18}\text{O}$  measurements, able to furnish the  $\text{H}_2$  density profile and the CO depletion, were carried out in cases where these were not available in the literature.

In section 2 of this paper, we outline our observational technique both for the  $\text{N}_2\text{H}^+$  and  $\text{N}_2\text{D}^+$  observations and for the dust continuum and  $\text{C}^{18}\text{O}$ . In section 3, we summarize our direct observational results, and in section 4 we derive physical and chemical quantities for the cores in our sample. In section 5, we discuss statistical correlations between the physical properties derived for our sample and in section 6, we summarize our conclusions.

## 2. Observations

### 2.1. The Sample

We have selected 31 cores to be observed in  $\text{N}_2\text{H}^+$  and  $\text{N}_2\text{D}^+$ . The criteria used in the sample selection were not completely homogeneous but we think the sample should be representative of evolved starless cores. “Evolved” in this context means that there is evidence for high density in the form either of strong  $\text{N}_2\text{H}^+(1-0)$  emission ( $\gtrsim 3 \text{ K km s}^{-1}$  in  $T_{\text{MB}}$  scale) or strong 1.2-mm dust continuum ( $\gtrsim 30 \text{ mJy}/(11'' \text{ beam})$ ) emission or both. The rationale here is that both of these criteria suggest a high central  $\text{H}_2$  column density and hence high central pressure, given that  $\text{N}_2\text{H}^+$  appears to well trace the dust (e.g. Tafalla et

al. 2002).

Of the 31 objects selected in this manner, 24 belong to an earlier map survey of  $\text{N}_2\text{H}^+$  and CS by Lee et al. (2001), aimed at detecting “extended” infall in starless cores through the comparison of the line profiles of optically thick (CS) and thin ( $\text{N}_2\text{H}^+$ ) tracers. We considered all cores in the Lee et al. (2001) sample showing strong  $\text{N}_2\text{H}^+(1-0)$  lines and compact morphology. Among these, 13 show infall asymmetry (i.e. CS spectra peaking at lower velocities than  $\text{N}_2\text{H}^+$ ), 7 show no asymmetry and 4 show outflow asymmetry.

Of the other 7 cores (L1495, L1400K, TMC1C, L1689A, B68, L328, GF5) in our sample some have been mapped in lines of  $\text{NH}_3$  (Benson & Myers 1989) and  $\text{N}_2\text{H}^+$  (Caselli et al. 2002c) and all have been mapped in dust continuum emission and show compact morphology and relatively high central number densities ( $n(\text{H}_2) \gtrsim 10^5 \text{ cm}^{-3}$ ; Bacmann et al. 2000; Shirley et al. 2000; Tafalla et al. 2002). Finally, the cores in our sample are nearby enough (within 250 pc), in order to spatially resolve the dense core nucleus. The total sample is listed in Table 1; columns 2, 3 and 4 show the J2000 coordinates and the distance in parsec, taken from the reference in column 5. In column 6 we specify if the core is isolated or embedded in a particular star forming region. Then in column 7 we give the total number of positions observed in both  $\text{N}_2\text{H}^+$  and  $\text{N}_2\text{D}^+$ . Finally in column 8 and 9, we report on the availability of a 1.2-mm map and of a  $\text{C}^{18}\text{O}$  map with the reference to it.

## 2.2. $\text{N}_2\text{H}^+$ and $\text{N}_2\text{D}^+$

The  $\text{N}_2\text{H}^+$  and  $\text{N}_2\text{D}^+$  observations were carried out between April 2002 and January 2003 using the IRAM 30-m telescope. We observed in frequency switch mode and we used the autocorrelator as the backend. Details on the telescope setting used are given in Table 2. The frequencies of  $\text{N}_2\text{H}^+(1-0)$ ,  $\text{N}_2\text{D}^+(2-1)$  and  $\text{N}_2\text{D}^+(3-2)$  were updated following the recent results of Dore et al. (2004). A new value for  $\text{N}_2\text{H}^+(3-2)$  frequency was calculated, first, evaluating the  $\text{N}_2\text{H}^+$  rotational constant ( $B = 46586.87546 \pm 0.00025 \text{ MHz}$ ) from the new  $\text{N}_2\text{H}^+(1-0)$  frequency determination (Dore et al. 2004) and then, using the centrifugal distortion constant from Verhoeve et al. (1990). In Table 2, we report the frequency of the  $F_1 F = 45 \rightarrow 34$  hyperfine component which has a relative intensity of 17.46%. The pointing and focus were checked approximately every two hours observing planets or quasars in continuum. The pointing corrections never exceeded  $4''$ . The intensity scale was converted to the main beam temperature according to the efficiencies reported in the IRAM 30-m web site<sup>1</sup>.

---

<sup>1</sup><http://www.iram.fr/IRAMES/index.htm>

We first observed the total sample at the peak position given either from previous  $\text{N}_2\text{H}^+$  observations (Lee et al. 2001) or from the dust maps (Bacmann et al. 2000). Then, we made a map of the cores which showed the strongest  $\text{N}_2\text{D}^+(2-1)$  lines: L1521F, L1544, TMC2, L183, OphD, L492, L429 and L694-2. TMC2 was mapped only in  $\text{N}_2\text{D}^+$  and we thus evaluate the ratio of  $\text{N}_2\text{H}^+$  and  $\text{N}_2\text{D}^+$  towards the only available position observed in  $\text{N}_2\text{H}^+$  (25" off the  $\text{N}_2\text{D}^+$  strongest position). The  $\text{N}_2\text{H}^+$  and  $\text{N}_2\text{D}^+$  maps towards L1495, L1517B, L1498, L1400K and L1512 were taken as part of a different project on starless cores aimed at determining the ionization degree (Caselli et al., in preparation); here we just use the  $\text{N}_2\text{H}^+$  and  $\text{N}_2\text{D}^+$  values at the dust peak (determined by Tafalla et al. 2002). The L1544 and L1521F data used in the present paper are taken from Caselli et al. (2002a) and Crapsi et al. (2004) respectively.

### 2.3. Dust continuum and $\text{C}^{18}\text{O}$

Millimeter continuum observations, taken with MAMBO (the IRAM 30-m bolometer), were already available in literature for 12 cores in our sample (L1544, OphD: Ward-Thompson et al. (1999); L1689B, L328, L429, GF5: Bacmann et al. (2000); L1498, L1495, L1517B, L1400K: Tafalla et al. (2002); L183: Pagani et al. (2003); L1521F: Crapsi et al. (2004); L694-2: Tafalla et al. in preparation). Moreover, a 1.2-mm map of B68 taken with SIMBA (the facility bolometer at SEST) was published in Bianchi et al. (2003). We obtained a 1.2-mm map of two more cores: TMC2 that presents high  $\text{N}_2\text{D}^+$  emission and L492 which has very strong  $\text{N}_2\text{H}^+(1-0)$  lines. Observations were carried out by the IRAM staff between January 2003 and February 2003 using the new 117-channel bolometer. The IRAM 30-m HPBW at 1.2 mm is approximately 11". The calibration error is estimated to be  $\sim 10\%$ . We mapped TMC2 in a  $7' \times 7'$  region scanning in the azimuthal direction at 5"/sec with a spacing between the scans of 9", reaching a sensitivity of 6 mJy/beam at the map center. The zenith optical depth, measured before and after the map, was 0.2. L492 was mapped in a  $3' \times 3'$  region scanning in the azimuthal direction at 5"/sec with a spacing between the scans of 8"; the RMS at map center is 5 mJy/beam. The zenith optical depth, measured before taking the map, was 0.2.

The data reduction (baseline fitting, sky-noise subtraction and regridding) was performed using the NIC program of the GAG software developed at IRAM and the Observatoire de Grenoble (Broguière et al. 2003).

In the same fashion, we observed the  $\text{C}^{18}\text{O}(1-0)$  and (2-1) for those cores where data were not already available in literature i.e. L183, L694-2, L492 and TMC2. We mapped in the on-the-fly mode in a region  $150'' \times 150''$  wide ( $200'' \times 300''$  for L183 and  $200'' \times 200''$  for

TMC2) scanning in the azimuthal direction. Both the separation between two scans and the separation between two dumps were 5''. C<sup>18</sup>O data were already available for L1544 (Caselli et al. 1999), OphD, L328, L429 (Bacmann et al. 2001), L1495, L1498, L1517B (Tafalla et al. 2002), B68 (Bergin et al. 2002) and L1521F (Crapsi et al. 2004).

### 3. Results

#### 3.1. Spectra at dust peak

In Figure 1 and 2, we show the observed spectra of N<sub>2</sub>H<sup>+</sup>(1–0) and N<sub>2</sub>D<sup>+</sup>(2–1) towards the core dust peaks. The cores where no line was detected were omitted. The data were reduced using CLASS, the line analysis program of the GAG software (Buisson et al. 2002). Notable in particular is the double peaked profile with an infall asymmetry observed in L1544 as well as the red shoulder or wing seen in several other sources (OphD, L694-2, L492, L1521F, TMC1-C). In general, these more “complex” profiles are more apparent in the sources where the N<sub>2</sub>D<sup>+</sup>(2–1) line is strong (see below), though there are exceptions (e.g. TMC1 which has a relatively broad N<sub>2</sub>H<sup>+</sup> line with “outflow asymmetry” but weak N<sub>2</sub>D<sup>+</sup>(2–1))<sup>2</sup>. The integrated intensities of these spectra plus the N<sub>2</sub>H<sup>+</sup>(3–2) and N<sub>2</sub>D<sup>+</sup>(3–2) are reported in Table 3. We also give there the offset of the N<sub>2</sub>D<sup>+</sup>(2–1) peak from the reference position given in Table 1. In our sample of 31 cores, we detected N<sub>2</sub>H<sup>+</sup>(1–0) emission with S/N>10 in 29 cores. L1689A and GF5, which have a weak detection, will not be considered further in this paper. We detected N<sub>2</sub>D<sup>+</sup>(2–1) lines with S/N higher than 10 in 10 cores (L1521F, TMC2, L1517B, L1544, L183, OphD, L492, L328, L429, L694); another 13 were detected with S/N higher than 4. In our calculations, as well as the error due to the RMS noise (shown in Table 3), we adopt a calibration uncertainty of 10% for N<sub>2</sub>H<sup>+</sup>(1–0) and 15% for N<sub>2</sub>D<sup>+</sup>(2–1).

From hyperfine structure fitting of the spectra in Figure 1 and 2, we derived the line parameters shown in Table 4. We report the observed LSR velocities and linewidths in the two species finding in the first approximation good agreement suggesting that we are sampling the same regions along the line of sight.

Total optical depth estimates are derived from a simultaneous fit to the hyperfine satellites assuming that hyperfine levels are populated proportional to their statistical weights. These results show that the total optical depth (i.e. the sum of the optical depths of the seven satellites) in N<sub>2</sub>H<sup>+</sup>(1–0) can reach values as high as 20; considering the hyperfine structure of

---

<sup>2</sup>The TMC1 position observed is close to the “CS peak”, see Pratap et al. (1997)

$\text{N}_2\text{H}^+(1-0)$ , a total optical depth of 20 means that the main component ( $F_1 F = 23 \rightarrow 12$ ), which has a fraction of 7/27 ( $\equiv 25.9\%$ ) of the total line strength, is often optically thick while the weakest satellite ( $F_1 F = 10 \rightarrow 11$ ) with an intrinsic line strength of 1/27 (or 3.7%) of the total transition strength is in almost all cases optically thin (its maximum opacity in our sample is 0.7, towards L183, L1521F and B68). We note, however, that the combination of excitation anomalies (non-LTE effects in the hyperfine levels populations, see Caselli et al. 1995) and highly non gaussian line profiles (e.g. L1544, B68, L492, L1521F, L694-2) increases the uncertainty in the opacity estimate from the simultaneous fitting of the hyperfine components. In fact, the fitting model adopted assumes constant abundance and excitation temperature along the line of sight and do not consider variations in velocity and linewidth. To crudely estimate the variations on the more complex spectra, we derived the opacity of the  $\text{N}_2\text{H}^+(1-0)$  spectra in B68 and L1544 by the fit of only a couple of hyperfines and repeating that for all the different couples. In this way, we found a scatter of a factor of 2 in the resulting opacities around the value derived by the simultaneous fit of all the 7 components.

The results of the hyperfine structure fitting of the high S/N ( $> 5$ ) 1mm spectra are reported in Table 5. We also show in Figure 3 the  $\text{C}^{18}\text{O}(1-0)$  and (2-1) spectra towards the peak of L1521F, L694-2, L183, TMC2 and L492. Integrated intensities and results of the gaussian fits for these observations are reported in Table 6.

### 3.2. Maps of individual sources

A detailed description of the maps obtained in this work can be found in the Appendix A, where we also analyse core shapes and kinematics (Appendix B) of individual objects. Here we briefly summarize the main results. Our new maps confirm the well known finding that  $\text{N}_2\text{H}^+$  and  $\text{N}_2\text{D}^+$  well trace the millimeter dust continuum emission, unlike CO (e.g. Caselli et al. 1999; Bergin et al. 2001; Tafalla et al. 2002). We also find that the majority of the cores are “cometary” in shape, suggesting that the cores have been either compressed by external agents or have moved relatively to the surrounding environment (but see Walsh & Myers 2004). In general, they do not show an axisymmetric morphology. Finally, we studied the kinematics in individual cores, evaluating the “total” and “local” velocity gradients and finding that only in one case (L694-2) the  $\text{N}_2\text{H}^+(1-0)$  line width increases toward the core center, indicating the presence of enhanced dynamical activity (likely due to infall), as already found in L1544 (Caselli et al. 2002a) and L1521F (Crapsi et al. 2004).

In the rest of the paper we concentrate on the physical and chemical parameters at the relative peak of the whole source sample.

## 4. Analysis

In this section, we derive the physical and chemical properties that can better discriminate the evolutionary status of a starless core, either in a chemical sense, as a more pronounced deuterium enrichment as well as a higher CO depletion factor, or for dynamical reasons, like the presence of a denser and more centrally concentrated H<sub>2</sub> distribution or broader N<sub>2</sub>H<sup>+</sup> line widths. We expect to characterize through these parameters the pre-stellar cores, i.e. the subset of starless cores that present enhanced chemical evolution and/or dynamical activity.

### 4.1. Column densities of N<sub>2</sub>H<sup>+</sup> and N<sub>2</sub>D<sup>+</sup> and the deuterium fractionation

The deuterium fractionation can be evaluated from observations of a hydrogen bearing molecule and one of its deuterated counterparts by calculating the ratio of their column densities. Recent work has made use of HCO<sup>+</sup>, H<sub>2</sub>CO, HNC, N<sub>2</sub>H<sup>+</sup> and NH<sub>3</sub>, and their single or multiple deuterated isotopomers, to evaluate this parameter in starless cores (Caselli et al. 1998; Roueff et al. 2000; Tiné et al. 2000; Bacmann et al. 2003; Caselli et al. 2002b; Hirota, Ikeda & Yamamoto 2003; Crapsi et al. 2004). One should note however, given the depletion of HCO<sup>+</sup> and H<sub>2</sub>CO in the core nucleus (Caselli et al. 2002b; Carey et al. 1998), that the deuterium fractionation estimated from this species is relative to an outer shell and not to the core nucleus.

In this work, we derived N<sub>2</sub>H<sup>+</sup> and N<sub>2</sub>D<sup>+</sup> column densities assuming a constant excitation temperature (the CTEX method: see appendix of Caselli et al. 2002b). The excitation temperature of N<sub>2</sub>H<sup>+</sup>(1–0) was derived from hyperfine fitting of the spectra with well constrained opacities ( $\tau/\sigma_\tau > 3$ , where the total optical depth  $\tau$  and its associated error  $\sigma_\tau$  have been derived assuming a constant excitation temperature for the hyperfine components; see also Table 4); otherwise the spectrum was assumed optically thin and the excitation temperature was set to 4.8 K (the average excitation temperature in our sample). The excitation temperature of N<sub>2</sub>D<sup>+</sup>(2–1) was set equal to that of N<sub>2</sub>H<sup>+</sup>(1–0) in those cases where the opacity was not well constrained. The effect of underestimating the N<sub>2</sub>D<sup>+</sup>(2–1) excitation temperature by e.g. 1 K would be the decrease of N(N<sub>2</sub>D<sup>+</sup>) of 30%. As noted above, in the case of N<sub>2</sub>H<sup>+</sup>, the optically thin assumption is often incorrect and hence we have used the intensity of the ( $F_1 F = 10 \rightarrow 11$ ) (weak) component normalized appropriately in order to estimate the J=0 column density.

The final result can be seen in Figure 4 where the N<sub>2</sub>H<sup>+</sup> column density is plotted versus the N<sub>2</sub>D<sup>+</sup> column density.

The estimated  $N(N_2D^+)/N(N_2H^+)$  ratio varies between 0.44 in Oph D and an upper limit of 0.02 in L1400K. It is noticeable that with the exception of OphD, all cores with  $N(N_2D^+)/N(N_2H^+)$  ratio above 0.10 have  $N_2H^+$  column densities above  $10^{13} \text{ cm}^{-2}$ , whereas cores with  $N(N_2D^+)/N(N_2H^+)$  lower than 0.10 have  $N(N_2H^+)$  lower than  $10^{13} \text{ cm}^{-2}$  (with a few exceptions). Thus, the impression from Figure 4 is that there is a trend in the sense that the  $N(N_2D^+)/N(N_2H^+)$  ratio correlates positively with  $N_2H^+$  column density. Table 7 summarize the above numbers.

We also determined the  $N_2H^+$  and  $N_2D^+$  column densities in the Large Velocity Gradient (LVG) approximation in those cores with high S/N  $N_2H^+$  and  $N_2D^+$ (3–2) spectra (see Appendix C). Results are shown in Table 8. The LVG column density determinations are found to agree with the CTEX values with a dispersion of 30%.

#### 4.2. The integrated CO depletion factor

The CO integrated depletion factor is the ratio of the CO canonical abundance ( $[CO]/[H_2] \equiv 9.5 \times 10^{-5}$ , Frerking et al. 1982) and the CO observed abundance. The CO observed abundance integrated along the line of sight can be calculated from the ratio of the CO column density and the  $H_2$  column density.  $C^{18}O$  is measured to be optically thin in some of the cores (L1521F, L183, L694-2, TMC2, L492) where  $C^{17}O$  observations are available. Optical depth was derived from the integrated intensity ratio of the two isotopomers assuming equal excitation temperature and the local interstellar medium relative abundance value (3.2, Wilson & Rood 1994). The maximum optical depth was measured to be 0.8 towards L1521F. Thus, for practical purposes, we assumed  $C^{18}O$  optically thin in all the cores. To derive  $N(CO)$  we used the CTEX approximation on the  $C^{18}O$  lines. As already shown in Caselli et al. (2002b) and Crapsi et al. (2004), this approach reduces the evaluation of the integrated CO depletion factor to the simple formula  $f_D = 0.085 \cdot \mathcal{F}_{1.2\text{mm}}/W_{C^{18}O}$ , where  $\mathcal{F}_{1.2\text{mm}}$  is the 1.2-mm observed brightness in  $\text{mJy beam}^{-1}$  and  $W_{C^{18}O}$  is the  $C^{18}O$  integrated intensity in  $\text{K km s}^{-1}$ .

The source of uncertainties in this technique are several and it is important to keep them in mind in the analysis of the results. First, the “canonical CO abundance” measured by different authors or in different objects varies by a factor of 2 (Lacy et al. 1994, Alves et al. 1999, Kramer et al. 1999). Second, one has to bear in mind that the integrated CO depletion factor is an average value along the line of sight, thus the local depletion factor in the nucleus of the core is much greater (see e.g. Caselli et al. 2002b; Crapsi et al. 2004).

The integrated depletion factors of L1689B, L328, OphD and L429 were already pub-

lished in Bacmann et al. (2002), that of L1544 in Caselli et al. (2002b) and that of L1521F in Crapsi et al. (2004). We evaluate the  $f_D$  values for L1495, L1498 and L1517B using the data published in Tafalla et al. (2002), for B68 using the  $C^{18}O(1-0)$  intensities published in Bergin et al. (2002) and the 1.2-mm continuum data published by Bianchi et al. (2003), for L183 using the 1.2-mm map of Pagani et al. (2003) and our  $C^{18}O$  observations, for L694-2 using the 1.2-mm map of Tafalla et al. (in preparation) and our  $C^{18}O$  observations and for TMC2 and L492 using the  $C^{18}O$  and the 1.2-mm maps from this paper. Results are shown in column 4 of Table 9.

### 4.3. $H_2$ volume density

The  $H_2$  column density can be derived from the millimeter continuum under the approximation of optically thin emission, constant temperature and constant emissivity of the dust at these wavelengths. The equation that relates the  $H_2$  column density to the 1.2-mm flux is:

$$N(H_2) = \frac{S_{1.2mm}}{B_\nu(T) \Omega_{beam} \kappa_{1.2mm} m},$$

where  $N(H_2)$  is the  $H_2$  column density,  $S_{1.2mm}$  is the flux density integrated over the solid angle  $\Omega_{beam}$ ,  $B_\nu(T)$  is the Planck function at temperature  $T$ ,  $\kappa_{1.2mm}$  is the dust opacity per unit mass and  $m$  the mean molecular mass. In our calculations, we assume a dust temperature of 10 K and a dust opacity of  $0.005 \text{ cm}^2 \text{ g}^{-1}$ . The assumption in the dust temperature is justified from the estimates obtained from  $NH_3$  (Tafalla et al. 2002) and  $H_2CO$  (Bacmann et al. 2002) observations in several cores of our sample. We note that the dust temperature is predicted to drop in the core nucleus (Evans et al. 2001; Zucconi et al. 2001); assuming a temperature of 8 K would determine an increase of the column density of a factor 1.5. We also remark that the dust opacity value, assumed following Andrè et al. (1996), suffers from an uncertainty of a factor of 2 (Henning, Michel & Stognienko 1995; Bianchi et al. 2003; Kramer et al. 2003).

In this work, we both collected 1.2-mm maps from the literature and observed new sources with the bolometers. In Table 9, we report the  $H_2$  volume density at the peak of L429 and L328 taken from Bacmann et al. (2000), of L1495, L1498, L1517B and L1544 from Tafalla et al. (2002), of OphD, L1689B from Ward-Thompson et al. (1999), of L694-2 from Harvey et al. (2003) (using their Bonnor-Ebert fit and changing  $\kappa_{1.2mm}$  to  $0.005 \text{ cm}^2 \text{ g}^{-1}$  for consistency), of L183 from Pagani et al. (2003) and of L1521F from Crapsi et al. (2004). All the central densities above were determined from 1.2-mm continuum data and using the same basic technique (i.e. a fit of the observed continuum emission starting from a volume

density model of the core). We remark that these estimates were obtained assuming spherical symmetry. A strong deviation of the density profile along the line of sight with respect to what is seen in the plane of the sky will cause errors in the volume density determination. For some of these cores other different estimates for the peak density are reported in literature; these were obtained starting from different data (molecular line or 850  $\mu\text{m}$  continuum) or using different techniques. In case of multiple estimates all done starting from 1.2-mm continuum data we adopted the most recent value: e.g. L1544 has three determinations of the density that were done from a 1.2-mm map:  $1.5 \times 10^6 \text{ cm}^{-3}$  by Ward-Thompson et al. (1999),  $4 \times 10^5 \text{ cm}^{-3}$  by Bacmann et al. (2000) and  $1.4 \times 10^6 \text{ cm}^{-3}$  by Tafalla et al. (2002); in this work we adopted the most recent determination from Tafalla et al. (2002).

The  $\text{H}_2$  central volume density at the TMC2, L492 and B68 peaks was evaluated with the same technique as for L1521F (Crapsi et al. 2004). We assumed the analytical model for the volume density given by Tafalla et al. (2002):  $n(\text{H}_2) = n_0 / (1 + (r/r_0)^\alpha)$ , where the central density ( $n_0$ ), the “flattened radius” ( $r_0$ ) and the steepness of the profile at large radii ( $\alpha$ ) are free parameters. Then, we searched for the best combination of parameters able to predict the observed continuum measurements. In this way we found at the peak of TMC2 a  $\text{H}_2$  density equal to  $3 \times 10^5 \text{ cm}^{-3}$ , while  $2.1 \times 10^5 \text{ cm}^{-3}$  is the measured density towards the L492 peak. B68 central density, derived from lower S/N data (and with worst angular resolution), was found to be  $8 \times 10^4 \text{ cm}^{-3}$  with large errorbars.

Volume densities were also derived using an LVG program (see Appendix C), whose results are summarized in Table 8. We found systematically lower central densities using the molecular data ( $\sim 3$  times less) than using the dust (as already found in L1544; see Caselli et al. 2002b), suggesting that  $\text{N}_2\text{H}^+ - \text{N}_2\text{D}^+$  may be probing a shell exterior to the high density nucleus (see Figure 17 in Appendix C). This indication is consistent with the idea that  $\text{N}_2$  could freeze-out for densities higher than  $5 \times 10^5 \text{ cm}^{-3}$  as suggested by Bergin et al. (2002) and Belloche & Andrè (2004). Keto et al. (2004) also found a similar result using  $\text{N}_2\text{H}^+$  data and suggest that a way to reconcile gas density estimates from dust observations with those from molecular line observations is to increase the dust mass opacity to  $\kappa = 0.04 \text{ cm}^2 \text{ g}^{-1}$ , value typical of fluffy aggregates with ice mantles. We underline that higher resolution observations are strongly needed to confirm this trend.

#### 4.4. Dust emission equivalent radius and aspect ratio

In starless cores the  $\text{H}_2$  density profile can be approximated by a region of roughly constant density followed by a power law decrease (Ward-Thompson et al. 1999; Bacmann et al. 2000; Tafalla et al. 2002); this behaviour is reflected in the 1.2-mm continuum emission.

Since the “flattened nucleus” is expected to become smaller with the ongoing of infall, its size gives us a measure of the relative contraction stage reached by the cores. Unfortunately each author uses different definitions for the size of the flattened region; thus, we have measured, for the 13 cores with a 1.2-mm map, the area within the 70% contour of the dust peak. We then translated this into a radius (reported as  $r_{70}$  in figures and tables) by evaluating the square root of this area divided by  $\pi$ . The resulting values are reported in column 5 of Table 9. This approach is useful for a relative comparison of the different cores. The choice of the 70% contour as threshold is justified by the fact that we wanted to limit the influence of the “cometary tail” (see Appendix B) on the  $r_{70}$  determination.

We also evaluated the aspect ratio of the dust emission measuring the major and minor axis size of the 50% contour and 70% contour (results are shown in column 6 and 7 of Table 9). We found that the axis ratio increases at lower contours in the more cometary cores, reaching values up to 2.5.

#### 4.5. The line asymmetry

The analysis of the line profile gives us clues on the core kinematics. In fact, motions along the line of sight combined with optical depth effect, molecular abundance variations and temperature gradients alter the line profile, causing departures from a Gaussian line shape. In particular, looking at the density peak, we expect a “blue shoulder” in case of outflow motions and a “red shoulder” in case of infall motions (see Evans 2002 for a review).

Here, we determine the degree of line asymmetry by calculating the line skewness, or the third momentum, of a distribution equivalent to the line profile. This is defined as  $\sum_{i=1}^N ((x_i - \bar{x})/\sigma_x)^3/N$  where  $\bar{x}$  and  $\sigma_x$  are the first and second moment of the same distribution and  $N$  is the total number of points (see e.g. Press et al. 1988). By definition, the third moment measures the deviation from a symmetric distribution, as the first moment furnishes its mean and the second yields its dispersion. It is a non-dimensional quantity and assumes positive values for distributions which have a “tail” in the values higher than the mean and negative values in the opposite case. We applied this analysis on the ( $F_1 F = 2\,2 \rightarrow 1\,1$ ) component of the  $\text{N}_2\text{H}^+$  (the fourth starting from the lower velocities). The “isolated” ( $F_1 F = 0\,1 \rightarrow 1\,2$ , the one at lowest velocity) and the “weak” ( $F_1 F = 1\,0 \rightarrow 1\,1$ , the one at highest velocity) components show approximately the same behaviour as this one in the very high signal to noise spectra (RMS  $< 0.03$  K with a  $0.063$  km s $^{-1}$  channel spacing); so, in order to enlarge the sample to spectra with slightly lower S/N (RMS  $< 0.1$  K), we used the data from the ( $F_1 F = 2\,2 \rightarrow 1\,1$ ) component which also provides a sufficient isolation from the other components even in the spectra with broadest line widths. Moreover, given

the role of the optical depth in the production of the asymmetric profiles, the ( $F_1 F = 22 \rightarrow 11$ ) component is supposed to have a more pronounced skewness than the other two components. Results are shown in Table 9. Eight cores show red-skewed “contracting” profiles, 6 cores show blue-skewed “expanding” profiles and 7 cores have symmetric profiles within the errorbars. Note that the line peak in the “contracting” profiles falls at lower velocities (or on the blue side) than  $\bar{x}$  whereas asymmetric profiles with outflow character are the reverse.

## 5. Discussion

In the following, we will discuss the relations between the quantities determined in the previous sections and compare them with simple theoretical expectations. We divide this section in two main parts: in the first we will concentrate on the prediction between deuterium fractionation and the other chemical and dynamical parameters derived in Section 4 while in the second we will cross-correlate only the parameters linked with the kinematical activity.

### 5.1. Deuterium Fractionation correlations

#### 5.1.1. Deuterium fractionation and CO depletion

An observational proof of the chemical model relating the deuterium fractionation with the CO depletion factor was given in Bacmann et al. (2003) using the ratio of D<sub>2</sub>CO over H<sub>2</sub>CO in a sample of 5 cores. Although D<sub>2</sub>CO and H<sub>2</sub>CO have been shown to deplete in the inner nucleus of the pre–stellar cores (Carey et al. 1998, Maret et al. 2004) hence they do not trace the very inner nucleus, these 5 cores (included in our sample) showed a good correlation between the CO depletion and the deuterium fractionation in H<sub>2</sub>CO with the exception of OphD.

Another possible test is to check for a correlation between the CO depletion factor and the deuterium fractionation within a given core. This test was performed in Crapsi et al. (2004) showing again an affirmative answer.

Here, we searched for a correlation between the integrated CO depletion factor and the deuterium fractionation in a subsample of 14 cores using the high density gas tracers N<sub>2</sub>H<sup>+</sup> and N<sub>2</sub>D<sup>+</sup> to derive the deuterium fractionation. The result is shown in Figure 5, where we denote by enclosed data points our ”candidate pre–stellar cores”, defined for the purpose of

this paper as having  $N(N_2D^+)/N(N_2H^+) \geq 0.1$ .

The correlation is not extremely tight (correlation coefficient 69%; 74% if only Taurus cores are considered) but indeed we can say that the cores that show higher CO depletions do also show higher deuterium fractionation. As in Bacmann et al. (2003), OphD seems to have “too much” deuterium fractionation compared to the CO depletion.

In Figure 5, we also show theoretical curves from simple chemical models based on that described by Caselli et al. (2002b). These models all assume that the gas and dust temperatures are constant across the core and equal to 10 K. The chemical network and chemical parameters are also the same in all the models: apart from  $H_2$ , the chemical network contains the three neutral species CO,  $N_2$ , and O which can freeze-out onto dust grains and return to the gas phase via thermal desorption or cosmic-ray impulsive heating (following the formulation of Hasegawa & Herbst 1993). On the other hand, the abundances of the molecular ions ( $N_2H^+$ ,  $HCO^+$ ,  $H_3O^+$ ,  $H_3^+$  and their (multiply) deuterated counterparts) are calculated in terms of the instantaneous abundances of the neutral species. This simplification is based on the fact that the “ion chemistry” time scale is much shorter than the depletion time scale (see Caselli et al. 2002b and Crapsi et al. 2004 for details). Here, we included the multiply deuterated forms of  $H_3^+$ , without any distinction among the ortho and para forms of molecular hydrogen and  $H_2D^+$  and without taking into account the so-called “back reactions” between e.g. ortho- $H_2$  and ortho- $H_2D^+$  (Gerlich et al. 2002), which limit the deuterium fractionation, as discussed in Walmsley et al. (2004). However, we adopted the new value of the rate coefficient for the proton-deuteron exchange reaction  $H_3^+ + HD \rightarrow H_2D^+ + H_2$  ( $3.5 \times 10^{-10} \text{ cm}^3 \text{ s}^{-1}$ ; Gerlich et al. 2002). The other parameters used are: the cosmic-ray ionization rate  $\zeta = 1.3 \times 10^{-17} \text{ s}^{-1}$ ; the CO,  $N_2$ , and O binding energies:  $E(\text{CO}) = 1210 \text{ K}$ ,  $E(N_2) = 800 \text{ K}$ , and  $E(\text{O}) = 650 \text{ K}$ <sup>3</sup>, respectively; the lower cutoff radius of the MRN (Mathis et al. 1977) distribution  $a_{\min} = 5 \times 10^{-6} \text{ cm}$ .

The different model predictions, denoted as  $n_1$ ,  $n_2$ ,  $n_3$ ,  $n_4$  and  $n_5$  in Figure 5, refer to model spherical clouds with different density structures, in (rough) analogy with the density structure of the model cloud undergoing infall, described by Ciolek & Basu (2000; hereafter CB), at successive evolutionary stages (from  $t_1 = 2.27 \text{ Myr}$  to  $t_5 = 2.684 \text{ Myr}$ , see CB). We remark that our calculations are in the steady state approximations so our model makes use of the density profile only and not of the time scale. We also note that the

---

<sup>3</sup>All the adopted parameters are the same as in Crapsi et al. 2004, with the exception of  $E(\text{O})$ , which is now 100 K lower than before. The decrease in this parameter is necessary to keep the deuterium fractionation at a similar level than in Crapsi et al. (2004), for the particular case of L1521F, after the inclusion of all the multiply deuterated forms of  $H_3^+$ . See also Caselli et al. 2002b for the importance of atomic oxygen in this simple chemical network.

CB model has cylindrical (rather than spherical) symmetry and we have neglected this fact assuming roughly the same dependence on spherical radius as that on cylindrical radius in CB. We assume that the density profiles are given by the analytical formula of Tafalla et al. (2002), with different values of the parameters (namely, the central density, the radius of the inner flat region, and the asymptotic power index) to approximately reproduce the density profiles of Figure 1a of CB. In particular, the central densities of the cores at each time are given by  $10^j \times 4.37 \times 10^3 \text{ cm}^{-3}$  (for  $j = 1, \dots, 5$ ) as in CB. The abundance profiles obtained in this way have then been converted in column densities via integration along the line of sight and successive convolution with a 2D gaussian, simulating observations with a HPBW of  $22''$ . From Figure 5 we note that the deuterium fractionation in  $\text{N}_2\text{H}^+$  as well as the observed CO depletion factor ( $f_{\text{D}}$ ) are predicted to increase with core evolution and actually explain the observed trend, although some scatter is expected in the data, given the different environments where they are immersed and their different formation histories. In particular, we expect magnetic field strength, amount of turbulence, external radiation field and external pressure to influence the evolution of a core. The result is that two cores with the same mass and same age could then be differently evolved depending on the characteristics of the surrounding star forming region. We note that most of the "pre-stellar" cores are found close to the  $n_3$  result, which, in the CB model, is the model of best agreement with the measured density profile of L1544. Therefore, we can conclude that the "pre-stellar core" condition,  $\text{N}(\text{N}_2\text{D}^+)/\text{N}(\text{N}_2\text{H}^+) \geq 0.1$ , is consistent with values of central densities  $\text{n}(\text{H}_2) \geq 10^6 \text{ cm}^{-3}$ , in agreement with  $\text{H}_2$  central densities measured from the dust in Section 4.3 for these cores.

We also searched for correlations between the depletion factor and the  $\text{H}_2$  column density finding a positive correlation (87% correlation coefficient; 90% for Taurus only) confirming the general chemical scenario about CO depletion (see Dalgarno & Lepp 1984; Roberts & Millar 2000; Bacmann et al. 2002). Several authors have investigated the chemical structure of pre-stellar cores, coupling together dynamical and chemical evolution with detailed models (Bergin & Langer 1997; Aikawa et al. 2001; Li et al. 2002; Shematovich et al. 2003). Deuterium and singly deuterated species were however only included in Aikawa et al. (2001) who were able to reasonably reproduce the observed molecular D/H ratios toward L1544, although the column density of  $\text{N}_2\text{H}^+$  was underestimated. Aikawa et al. (2003) overcame this problem adding surface chemistry to their models. Surface processes significantly enhanced the production of the parent molecule  $\text{N}_2$ , increasing the  $\text{N}_2\text{H}^+$  column density to the observed values.

More recently, Roberts et al. (2004) studied the chemistry of pre-stellar cores including multiply deuterated species but neglecting the dynamical evolution. For the particular cases of L1544 and OphD they found  $\text{N}(\text{N}_2\text{D}^+)/\text{N}(\text{N}_2\text{H}^+)$  column density ratios significantly (fac-

tor of about 5) larger than the observed values, suggesting that the deuterium fractionation process is probably too efficient in their models. Possible causes of this disagreement are: (i) the exclusion of the so-called back reactions of deuterated isotopomers of  $H_3^+$  with ortho- $H_2$  (Gerlich et al. 2002), still not accurate at low temperature, which may lower the molecular D/H ratios (Walmsley et al. 2004); (ii) the use of large (radius = 0.1  $\mu m$ ) dust grains in the chemical network, which underestimates the recombination of molecular ions compared to models where a population of smaller grains is present or where a MRN size distribution of dust particles is considered; (iii) the use of UMIST rates, which produce  $H_3^+$  and analogues more efficiently than the "New Standard Model" from the Ohio–State University (see Roberts et al. 2004 for details).

### 5.1.2. Deuterium fractionation vs. $H_2$ central density, dust equivalent radius, $N_2H^+$ line width and $N_2H^+$ line skewness

In theoretical simulations, we expect an increase of the central  $n(H_2)$  density and a decrease of  $r_{70}$ , the equivalent radius of the flat region, with the ongoing contraction (e.g. Lizano & Shu 1989; Foster & Chevalier 1993; Ciolek & Mouschovias 1995; Li 1999). Those two parameters can be considered as indicators of "dynamical evolution"; here we cross-correlate them with the deuterium fractionation.

From Figure 6 panel a) one can see that there is a positive correlation between  $N(N_2D^+)/N(N_2H^+)$  and  $n(H_2)$  apart from OphD and L1521F which show opposite behaviours from the rest of the cores. Six of our pre–stellar cores candidates have  $H_2$  volume densities above the average ( $5.1 \times 10^5 \text{ cm}^{-3}$ ), and all of these show increases in deuterium fractionation above the average. Our estimate of the volume density depends on the assumed spherical geometry, hence we also considered the correlation between the deuterium fractionation and the  $H_2$  column density. While the general trend remained the same the peculiarity of OphD and L1521F becomes more marked.

We check, here, the relative variation of the flattened region in the 13 cores for which we have the 1.2-mm map. Having treated all the cores in a consistent way allows us to consider the differences in  $r_{70}$  real and not due to differences in the adopted fitting model. The correlation between deuterium fractionation and  $r_{70}$  is shown in Figure 6 panel b). A close relationship of the flattened radius with the deuterium fractionation is not found. OphD shows the biggest variation from this picture but one should notice the presence of a second peak inside its 70% contour. It is thus possible that the OphD equivalent radius is overestimated. A similar argument holds for L183. Limiting the sample to the Taurus cores

significantly tightens the correlation, increasing the correlation coefficient from 1% to 64%. Once again, this result suggests that cores embedded in different environments (e.g. external radiation field) hardly represent a homogeneous sample where to study evolutionary trends.

Caselli et al. (2002a) showed that in L1544 there was a definite trend for the  $\text{N}_2\text{H}^+$  and  $\text{N}_2\text{D}^+$  linewidths to increase towards the high density region. This result was interpreted as a sign of increasing infall activity towards the center. The same trend, although less marked, is seen in L1521F (Crapsi et al. 2004).

In this fashion, we take here the  $\text{N}_2\text{H}^+$  linewidth as an indicator of infall activity and thus proximity to the critical state for dynamical collapse and we check if the cores that had larger linewidths are the same with the largest  $\text{N}(\text{N}_2\text{D}^+)/\text{N}(\text{N}_2\text{H}^+)$  ratio, to search for links between the physical and chemical evolution. The result is in Figure 6 panel c). In our sample we do not see any correlation for larger linewidth in the nucleus of cores with larger deuterium fractionation. In particular, we note that L328 shows broad lines but low  $\text{N}(\text{N}_2\text{D}^+)/\text{N}(\text{N}_2\text{H}^+)$  and OphD which has the opposite behaviour. The two broadest line cores, L328 and L429, have both spectra with flat tops and blue skewed asymmetry (see Sect. 4.5), suggesting that their lines could be broadened for reasons other than infall. We attempted to go round the environmental differences, as a source of scatter for the correlation, limiting the sample to the Taurus cores only; in this case the correlation coefficient increases from 22% to 40%.

We point out that the above correlation does not make any distinction between cores which do and do not show evidences of central infall (through the  $\text{N}_2\text{H}^+(1-0)$  line width broadening toward the dust peak position, or with the presence of “red shoulders”), so that the different line widths observed in the cores of the present sample may simply arise from different amounts of turbulence in their interiors or other type of motions (e.g. expansion or oscillations) along the line of sight.

We also try to correlate the line skewness with the  $\text{N}(\text{N}_2\text{D}^+)/\text{N}(\text{N}_2\text{H}^+)$  ratio in Figure 6 panel d). Also in this case there is a general agreement with the proposed idea that cores with higher deuterium fractionation show also signs of kinematical evolution. The main exceptions in this case are given by L429 on one hand and by TMC1C and L492 on the other. It is interesting to note that the correlation between the  $\text{N}(\text{N}_2\text{D}^+)/\text{N}(\text{N}_2\text{H}^+)$  and the line asymmetry is more tight than that with the line width.

### 5.1.3. Deuterium fractionation and extended infall

Lee et al. (1999, 2001 and 2004) in a series of papers conducted a search for infall motions towards a sample of 70 starless cores. Infall motions were identified through the presence of velocity shifts between high density tracers ( $\text{N}_2\text{H}^+(1-0)$  probing densities up to a few  $10^6 \text{ cm}^{-3}$ ) and low density tracers (CS(2-1) tracing the gas up to  $\sim 10^4 \text{ cm}^{-3}$ ) and through the observation of double peaked self-absorbed optically thick lines whose blue peak was brighter than the red peak (see Lee et al. 2004). Given the CS depletion in the inner core, those measurements gauge the infall of the external envelope only.

Twentyfour cores in our sample were observed also in the Lee et al. papers (2001, 2004), including our chemically evolved candidates L1544, L1521F, L694-2, L183, L429, TMC2 and OphD (there known as L1696A). Considering now only this common subsample, Lee et al. (2004) found that 12 of these cores show infall signatures in at least 3 of the 7 tests they performed on CS,  $\text{DCO}^+$  and  $\text{N}_2\text{H}^+$  lines, thus they are consider strong infall candidates. All our chemically evolved candidates ( $\text{N}(\text{N}_2\text{D}^+)/\text{N}(\text{N}_2\text{H}^+) > 0.1$ ) (but OphD which was not studied with all the techniques by Lee et al. 2004) were identified as strong infall candidates by the Lee et al. (2004) analysis. This seems to show that our chemically evolved candidates, the majority of which show clear signs of central infall, are a subsample of the cores undergoing extended contraction.

We also performed a direct comparison between one of the infall indicators in Lee et al. (2004),  $\delta V_{\text{DCO}^+}$  ( $\equiv (V_{\text{DCO}^+} - V_{\text{N}_2\text{H}^+})/\Delta V_{\text{N}_2\text{H}^+}$ ), and our  $\text{N}_2\text{H}^+(1-0)$  skewness on a common subsample of 15 cores. We find a very good agreement between those two parameters with only two cases where they give a different indication: L429 which has significant outflow signature in the  $\text{N}_2\text{H}^+(1-0)$  skewness but marginal infall indication in  $\delta V_{\text{DCO}^+}$  and L183 which has a very strong outflow behaviour in the  $\delta V_{\text{DCO}^+}$  wheres it shows an infall profile in our  $\text{N}_2\text{H}^+(1-0)$  spectra. For the 13 remaining cores the two indicators correlate with a 70% correlation coefficient.

## 5.2. Dynamical parameters correlations

We cross correlated our “kinematic activity” indicators the  $\text{N}_2\text{H}^+(1-0)$  linewidth, the radius of the flattened region, the  $\text{H}_2$  column density and the  $\text{N}_2\text{H}^+(1-0)$  line asymmetry, to see whether they give a consistent information. The result is encouraging. We can in fact see in panel a) of Figure 7 that  $r_{70}$  is anti correlated with  $\text{N}_2\text{H}^+(1-0)$  line width (correlation coefficient 67%, 86% limiting to Taurus cores); note that even cores that in the other plots do not behave like the rest of the sample (OphD and L328) lie here in the common trend.

In panel b) of Figure 7, we find that, with the notable exception of L328 and L429, the  $\text{N}_2\text{H}^+(1-0)$  line width correlates fairly well with the  $\text{H}_2$  central density (correlation coefficient 20% for the total sample; 64% without L328 and L429; 94% for only the Taurus cores).

In the picture given in Section 5.1.2, the cores with strong motions along the line of sight should show stronger asymmetries and broader lines towards the core peak. In Figure 7 panel c), we plotted the relation between the width and the skewness of the  $\text{N}_2\text{H}^+$  line. Although again a tight correlation is not found we can see that there is a general trend of increased skewness in broader spectra. Remarkable exceptions are constituted by OphD and TMC1-C having narrow lines strongly skewed towards the red and by L429 and L328 which have the broadest lines in the sample but do not show any infall asymmetry. Also in this case, limiting the sample to Taurus cores, the correlation coefficient increases from 2% to 21%.

### 5.2.1. Line width and aspect ratio

The fact that the majority of the cores in our sample (see Figure 14 in Appendix B) show large departures from spherical symmetry has considerable significance for our understanding of the dynamics of these objects. Core shape could for example reflect the magnetic field structure and indeed several of the cores in our sample show linear polarization of around 5-10% (e.g. Crutcher et al. 2004) suggesting magnetic fields of order  $100 \mu\text{G}$ . However, the observed structures could also be a consequence of dynamical interactions with the core surroundings as is suggested by the observed “cometary” shapes. It is natural therefore to search for kinematic evidence in our  $\text{N}_2\text{H}^+$  maps which either excludes or favors one of these scenarios.

There are various possible kinematic probes including the observed velocity field but the simplest is to check for a correlation between line width and aspect ratio. Here the interpretation depends considerably on whether the true core shape is “close to oblate” or “close to prolate” (see e.g. Jones and Basu 2002, Curry 2002 who have attempted to decide this on the basis of the statistics of observed aspect ratios). Present results are inconclusive and we conclude that one must consider both possibilities.

In either case, if cores are magnetically dominated, motion along the field lines will be facilitated. We would expect that in such cases, motions will predominantly be parallel to the axis of symmetry and hence for oblate cores, one might expect the largest line widths for face-on circular sources and for prolate cores for end-on (also circular) objects. On the

other hand, ambipolar diffusion necessarily occurs across field lines and this will have the opposite effect. Thus for example, edge on oblate cores will have the largest linewidth. In fact, Ciolek & Basu (2000) have provided predictions for how the velocity field due to this latter process might appear in L1544 and Caselli et al. (2002a) showed that the observations were roughly consistent with the model for this object.

However, this does not seem to be the case in L1521F (Crapsi et al. 2004) and also not in a more general sample of cores as shown in Figure 7 panel d) where we plot the  $\text{N}_2\text{H}^+(1-0)$  linewidth against aspect ratio from the mm continuum maps. There is no clear trend in this plot and clearly a larger sample is needed. However, our results do not give evidence that in general there are increased linewidths towards elongated core nuclei as one might expect on the basis of models such as those of Ciolek & Basu (2002). On the other hand, our results also do not seem to favor the models of Curry and Stahler (2001) which suggest that initially elongated structures should become more spherical as they evolve due to ambipolar diffusion. We conclude that it would be useful to have more detailed predictions for model pre–stellar cores of the evolution with time of both the linewidth and the velocity field.

### 5.3. Associated properties

We have shown in this section a series of properties which we think can be associated to an evolved stage of the starless cores either because of enhanced chemical activity or because of an advanced kinematical process.

Even though we did not find tight one-to-one correlations between the numerical values it appears that these properties globally isolate a group of cores which looks peculiar from the rest of the sample. We summarize these characteristics of the evolved starless cores, or pre–stellar cores in Table 10. L1544 and L1521F were found to be more evolved than the “average” core in each test we performed, while L183, L429 and L694-2 failed just one test and can be considered strong candidate for pre–stellar core as well. Other cases, such as OphD and TMC2, are more doubtful.

In presence of an unbiased survey and assuming that all the cores will eventually form a star, one could attempt to estimate the duration for the pre–stellar core phase dividing the number of pre–stellar core candidates by the total number of objects in the sample. Since our main selection criterion stated that only the sources with stronger  $\text{N}_2\text{H}^+(1-0)$  observations (in the Lee et al. (2001) sample) or stronger dust emission-absorption (in the Bacmann et al. (2000) sample) were observed, we cannot consider our survey unbiased. Nevertheless, taking the number of  $\text{N}_2\text{H}^+$ –detected cores within 250 pc (49) in the Lee et al. (1999) sample

as representative of the total number of the  $\text{N}_2\text{H}^+$ –bright cores and supposing that L1544, L1521F, L183, L429, L694-2, OphD and TMC2 are the only pre–stellar cores observable in this sample, we can derive a duration of the pre–stellar phase equal to 7/49, or  $\sim 14\%$  of the lifetime of a core since it started to be observable in  $\text{N}_2\text{H}^+$ . Taking the smallest central density observed in our sample (B68:  $n(\text{H}_2) \sim 8 \times 10^4 \text{ cm}^{-3}$ ) as the threshold for  $\text{N}_2\text{H}^+$  emission, we can derive a lifetime of a  $\text{N}_2\text{H}^+$ –bright core of  $\sim 0.4$  Myr (using the Ciolek & Basu 2000 ambipolar diffusion models) hence the pre–stellar core phase should last around 60000 yr. An alternative estimate can be made evaluating the free-fall time for the threshold density for a pre–stellar core ( $n(\text{H}_2) \sim 5.1 \times 10^5$ ) resulting in a duration of  $\sim 60000$  yr. The pre–stellar cores lifetime can also be estimated from the comparison with the estimated time spent as a Class 0 protostar ( $\sim 2 \times 10^4$  yr Visser et al. 2002). From André et al. (1999) and Visser et al. (2002), we derive a total number of 11 Class 0 protostars within 250 pc. This, compared to the 7 evolved cores found in this work gives a duration of the pre–stellar phase of  $\sim 10000$  yr, shorter than the estimates above. However, we feel that this discrepancy merely reflects the great uncertainties in both estimates.

## 6. Conclusions

We collected a set of  $\text{N}_2\text{H}^+$ ,  $\text{N}_2\text{D}^+$ ,  $\text{C}^{18}\text{O}$  and 1.2-mm continuum observations using the IRAM 30-m for a sample of 31 starless cores, completing literature data with new observations. We retrieved from these data chemical and kinematical parameters supposed to discriminate young from more evolved cores such as: deuterium fractionation, integrated CO depletion factor,  $\text{H}_2$  density,  $\text{N}_2\text{H}^+$  line width and line asymmetry. Our conclusions are summarized below:

1. We attempted several correlation between the chemical evolution indicators (deuterium fractionation, integrated CO depletion factor and  $\text{N}_2\text{H}^+$  and  $\text{N}_2\text{D}^+$  column density) and properties of dynamically evolved cores (such as  $\text{H}_2$  volume density, line width and asymmetry and size of the flattened region). Although we did not find very tight dependences between these quantities, we recognized that all these properties, as a whole more than taken singularly, draw from the total sample those cores with an enhanced state of evolution. As can be seen from Table 10, we find that, compared to the total sample, L1544, L1521F, L183, L429, L694-2, OphD and TMC2 globally show:

- higher  $\text{N}_2\text{H}^+$  column density
- higher  $\text{N}_2\text{D}^+$  column density
- higher  $\text{N}(\text{N}_2\text{D}^+)/\text{N}(\text{N}_2\text{H}^+)$  abundance ratio

- higher H<sub>2</sub> column density
- higher integrated CO depletion factor
- broader N<sub>2</sub>H<sup>+</sup> lines
- smaller flattened radius
- stronger infall asymmetries

with some exceptions in each category.

2. Limiting the sample to the cores belonging to the Taurus Molecular Cloud tightens the correlations, probably by diminishing possible effects due to environmental differences such as magnetic field strength, amount of turbulence, external radiation field and external pressure.

3. The picture emerging from the observations is consistent with predictions of chemical models accounting for molecular freeze out, where cores with higher central densities show a lower fraction of CO in the gas phase and a correspondingly larger deuterium enrichment in the core nucleus.

4. N<sub>2</sub>D<sup>+</sup> and N<sub>2</sub>H<sup>+</sup> emissions, unlike C<sup>18</sup>O peak very close to the dust continuum maxima in the mapped cores, confirming the fact that those species probe better the conditions of the high density gas. Moreover, the maps of N<sub>2</sub>D<sup>+</sup> and of N<sub>2</sub>H<sup>+</sup>(3–2) were found to be systematically smaller than the N<sub>2</sub>H<sup>+</sup>(1–0) ones in all the mapped cores consistent with the idea that these trace better the high density nucleus. We note that central H<sub>2</sub> densities evaluated from the dust emission were found systematically larger than those calculated from LVG modeling of N<sub>2</sub>H<sup>+</sup> and N<sub>2</sub>D<sup>+</sup> data, suggesting that depletion of N<sub>2</sub> could possibly occur at the highest density peak, although finer resolution data are needed to confirm this effect.

5. The decrease of line-width towards the edge observed in L1544 (Caselli et al. 2002a) and L1521F (Crapsi et al. 2004) has been confirmed in only core (L694-2) with supposedly the same degree of evolution.

We would like to thank the IRAM 30-m staff for help during the observations. We gratefully acknowledge Philippe André, Aurore Bacmann, Simone Bianchi and Laurent Pagani for providing us with electronic versions of their 1.2-mm data. We also thank Luca Dore for communicating new frequency determinations. A.C. was partly supported by NASA “Origins of Solar System Grant” (NAG 5-13050). P.C. and C.M.W. acknowledge support from the MIUR grant “Dust and molecules in astrophysical environments”. C.W.L. acknowledges

supports from the Basic Research Program (KOSEF R01-2003-000-10513-0) of the Korea Science and Engineering Foundation.

## A. Maps

Figures 8 to 13 show maps towards L183, OphD, L429, TMC2, L492 and L694-2, which, together with L1544 and L1521F, stand out from the rest of the sample as having very bright  $\text{N}_2\text{D}^+(2-1)$  lines. Similar maps for L1544 can be found in Caselli et al. (2002a) and Tafalla et al. (2002) and in Crapsi et al. (2004) for L1521F. The  $\text{N}_2\text{H}^+ - \text{N}_2\text{D}^+$  data shown in Figures 8-11 were all convolved with a  $26''$  beam in order to reach the same spatial resolution as the  $\text{N}_2\text{H}^+(1-0)$  data and make the comparison easier. The  $\text{N}_2\text{H}^+(1-0)$  map of TMC2 (Figure 13) was kept with the original FCRAO resolution ( $54''$ ), while we have not smoothed the  $\text{N}_2\text{D}^+(2-1)$  map of L492 (Figure 12) because of the small extension of it. Similarly, all the 1.2-mm maps were smoothed to a  $22''$  resolution, the beamsize of the IRAM 30-m at the  $\text{C}^{18}\text{O}(1-0)$  frequencies.

The most evident feature of Figures 8 to 13 is that the  $\text{C}^{18}\text{O}$  does not trace the dust continuum while the  $\text{N}_2\text{H}^+$  and  $\text{N}_2\text{D}^+$  emission morphology is similar to that of the dust, as already shown by several authors (e.g Caselli et al. 1999; Bergin et al. 2001; Tafalla et al. 2002). While this is true for L1544, L1521F, L429, L694-2 and OphD, there are differences between the 1.2-mm map and the  $\text{N}_2\text{H}^+ - \text{N}_2\text{D}^+$  maps for L183 and TMC2. For example, the L183 dust emission peaks  $30''$  to the south of  $\text{N}_2\text{H}^+(1-0)$  and, especially,  $\text{N}_2\text{D}^+(2-1)$ .

TMC2 shows an even more complex situation, in fact the 1.2-mm maps revealed much more structure than the  $\text{N}_2\text{H}^+(1-0)$  map of Caselli et al. (2002c) led us to believe. Whereas we found a local 1.2-mm peak next to the  $\text{N}_2\text{H}^+(1-0)$  one, we also found brighter peaks of the dust emission in regions where the  $\text{N}_2\text{H}^+(1-0)$  is fainter. Note that the  $\text{N}_2\text{H}^+$  map in Figure 13 has a lower angular resolution (HPBW =  $54''$ ) than in the other sources; smoothing the dust continuum map to this resolution does not help to reconcile the two emissions, so we present here the 1.2-mm map with the same resolution as in the other cores (i.e.  $22''$ ). We also add in Figure 13 the position of a few radio stars and of a couple of IRAS point sources; the presence of these objects could explain the discrepancy between the  $\text{N}_2\text{H}^+$  and the dust maps.

Another common feature clearly seen throughout Figures 8 to 13 is that the  $\text{N}_2\text{D}^+$  maps are systematically smaller than the  $\text{N}_2\text{H}^+$  ones (see Table 11). This could indicate that the deuterated species are better tracers of the core nucleus. A similar behaviour is seen when the higher transitions maps are compared with those at lower  $J$ ; this may be caused by the increase in density towards map center.

In OphD (see Figure 10), we note the presence of two nuclei embedded in the same envelope; both have a similar brightness in the 1.2-mm continuum although they have a very different intensity in the  $\text{N}_2\text{H}^+(1-0)$ ,  $\text{N}_2\text{D}^+(2-1)$  and  $\text{N}_2\text{D}^+(3-2)$  (the  $\text{N}_2\text{H}^+(3-2)$  has poor

S/N towards the NE core). The relative intensity of the two nuclei decreases going from the lowest density tracer ( $\text{N}_2\text{H}^+(1-0)$ ) to the highest density one ( $\text{N}_2\text{D}^+(3-2)$ ), suggesting that the SW core is more centrally peaked than the NE one.

## B. Core shapes and kinematics

We underline a marked tendency of the starless cores for having the dust emission peak shifted relative to the centroid of the cores. In Figure 14, we attempt a classification of the shape of the starless cores evaluating a parameter able to quantify the degree of “cometariness” or how much the dust peak is shifted relative to the lower contours of the map. We evaluated the centroid of the map as the mean position of the points within the 50% contour and defined the degree of “cometariness” as the distance between this and the dust peak in units of  $r_{70}$ , the equivalent radius of the core. OphD and TMC2 were not included in this classification since they harbour multiple peaks within their 50% contour (see Figures 10 and 13) thus the “cometariness” parameter is meaningless. From this small subsample we do not notice any clear correspondence between a more marked cometary shape and other kinematical properties of the core (e.g.  $\text{H}_2$  density,  $\text{N}_2\text{H}^+(1-0)$  line-width or  $r_{70}$ ).

Using the  $\text{N}_2\text{H}^+(1-0)$  velocities from the hyperfine structure fitting, we found strong velocity variations in L183 ( $0.23 \text{ km s}^{-1}$  in a  $0.16 \text{ pc}$  length) and OphD ( $0.19 \text{ km s}^{-1}$  in a  $0.12 \text{ pc}$  length), while a smaller variation ( $0.07 \text{ km s}^{-1}$  in a  $0.1 \text{ pc}$  length) was found in L694-2 and constant velocity fields were seen in the inner  $0.08 \text{ pc}$  of L429 and L492. We evaluated the total velocity gradients of these cores under the assumption of solid body rotation (see Goodman et al. (1993)). The magnitudes and the direction of the velocity gradients are reported in column 1 and 2 of Table 12. These calculations agree with the velocity variations seen across the cores.

Local velocity gradients, evaluated in  $3 \times 3$  adjacent points, were also calculated towards these cores (see Caselli et al. 2002a for details on the procedure). The analysis was performed on regredded data and results are shown in Figure 15 and Table 12. L183 and OphD present strong motions and a regular velocity field. L429 and L492 show very little motion in the inner parts but larger gradients at the edge of the map with arrows pointing in different directions in different side of the cores, explaining the absence of velocity variation in the inner part and the small total velocity gradient. Finally, L694-2 shows the smallest local gradients with a regular velocity field only in the inner part.

Using the  $\text{N}_2\text{H}^+(1-0)$  and  $\text{N}_2\text{D}^+(2-1)$  maps, we also checked for the presence of linewidth gradients in L694-2, OphD, L183, L429 and L492 in the same fashion as for L1544 (Caselli

et al. 2002a), B68 (Lada et al. 2002) and L1521F (Crapsi et al. 2004). From figure 16, we find that only L694-2 shows the linewidth decrease that was evidenced in L1521F and L1544, while a marginal similarity is found in the first 50'' around OphD and in the northern part of L492. The opposite behaviour is seen in L429 and L183 (as found in B68). The  $N_2D^+(2-1)$  linewidths evidenced the same behaviour as in figure 16.

### C. Density determination in the LVG approximation

The Large Velocity Gradient (LVG) approximation simplifies the radiative transfer treatment assuming that a photon produced in a contracting or expanding cloud is reabsorbed locally and that the local velocity gradient is much larger than the ratio of linewidth to cloud size. In addition, one normally assumes homogeneous and isothermal conditions. Assuming a temperature of 10 K, we have used this approximation, with collisional rates from Green (1975) to compute level populations for  $N_2H^+$  and  $N_2D^+$  and to predict line intensities for these species as a function of density and species column density. We then compared the model predictions with the observed  $N_2H^+(3-2)/N_2H^+(1-0)$  intensity ratio and the  $N_2H^+(1-0)$  integrated intensity (or the  $N_2D^+(3-2)/N_2D^+(2-1)$  and  $N_2D^+(2-1)$  intensity) exploiting the fact that the former is mainly sensitive to  $n(H_2)$  and the latter to the  $N_2H^+(N_2D^+)$  column density. Our results are extremely sensitive to the intensity of the two 3–2 transitions and we hence confine our discussion to the 8 cores with  $S/N > 5$  in the 1 mm lines. An extra constraint comes from the total  $\tau$  of  $N_2H^+(1-0)$  ( $N_2D^+(2-1)$ ). Note that, given the small opacities found in  $N_2D^+(2-1)$  (and in many  $N_2H^+(1-0)$  spectra), the  $\tau$  has little influence on the  $n(H_2)$  determination, whereas it is a useful constraint for column density.

In Table 8, we summarize the results of the LVG calculations. The ratio of the  $N_2H^+ - N_2D^+$  column densities inferred from LVG and the relative value found in the CTEX approximation have an arithmetic mean value of 0.9 and a dispersion of 25%. Thus, the LVG results are consistent with the column densities derived assuming a constant rotational temperature.

It is interesting to note that the  $H_2$  densities derived from the molecular data are systematically smaller (a factor of  $\sim 3$ ) than those derived from the dust observations (see Figure 17). The differences between the two determinations diminish in the low density cores (a factor of  $\sim 2$ ). These differences may partially be due to our assumptions concerning the dust mm opacity and temperature (see Galli et al. 2002 for a discussion of the latter and Bianchi et al. 2003 for a discussion of the former). Another possibility is that depletion of  $N_2$  (and hence of  $N_2H^+$  and  $N_2D^+$ ) may occur in regions with density higher than  $5 \times 10^5 \text{ cm}^{-3}$  (see also Caselli et al. 1999, Bergin et al. 2001, Caselli et al. 2003, Crapsi et al. 2004, Belloche & Andrè 2004). In this latter case, one would expect differences between maps of

$\text{N}_2\text{H}^+$  and dust continuum (one possible example could be L183, see Appendix A). We note also that there is a hint in our data that densities derived from  $\text{N}_2\text{D}^+$  are systematically higher than those from  $\text{N}_2\text{H}^+$  and this again may be consistent with a hole caused by  $\text{N}_2$  freeze-out. However, we stress that these trends need confirmation and that measurements with higher sensitivity and angular resolution are needed.

## REFERENCES

Aikawa, Y., Ohashi, N., Inutsuka, S., Herbst, E., & Takakuwa, S. 2001, *ApJ*, 552, 639

Aikawa, Y., Ohashi, N., & Herbst, E. 2003, *ApJ*, 593, 906

Alves, J., Lada, C. J., & Lada, E. A. 1999, *ApJ*, 515, 265

André, P., Ward-Thompson, D., Motte, F. 1996, *A&A*, 314, 625

André, P., Ward-Thompson, D., & Barsony, M. 2000, *Protostars and Planets IV*, 59

Bacmann, A., André, P., Puget, J.-L., Abergel, A., Bontemps, S., & Ward-Thompson, D. 2000, *A&A*, 361, 555

Bacmann, A., Lefloch, B., Ceccarelli, C., Castets, A., Steinacker, J., & Loinard, L. 2002, *A&A*, 389, L6

Bacmann, A., Lefloch, B., Ceccarelli, C., Steinacker, J., Castets, A., Loinard, L. 2003, *ApJ*, 585, L55

Belloche, A. & André, P. 2004, *A&A*, 419, L35

Benson, P. J. & Myers, P. C. 1989, *ApJS*, 71, 89

Bergin, E. A. & Langer, W. D. 1997, *ApJ*, 486, 316

Bergin, E. A., Ciardi, D. R., Lada, C. J., Alves, J., & Lada, E. A. 2001, *ApJ*, 557, 209

Bergin, E. A., Alves, J., Huard, T., & Lada, C. J. 2002, *ApJ*, 570, L101

Bianchi, S., Gonçalves, J., Albrecht, M., Caselli, P., Chini, R., Galli, D., & Walmsley, M. 2003, *A&A*, 399, L43

Broguière, D., Neri, R., Sievers, A., & Wiesemeyer, H. 2003, NIC Bolometer Users Guide

Buisson G., Desbats L., Duvert G., Forveille T., Gras R., Guilloteau S., Lucas R., & Valiron P. 2002, CLASS manual

Carey, S. J., Clark, F. O., Egan, M. P., Price, S. D., Shipman, R. F., & Kuchar, T. A. 1998, *ApJ*, 508, 721

Caselli, P., Myers, P. C., Thaddeus, P. 1995, *ApJ*, 455, L77

Caselli, P., Walmsley, C. M., Terzieva, R., & Herbst, E. 1998, *ApJ*, 499, 234

Caselli, P., Walmsley, C. M., Tafalla, M., Dore, L., & Myers, P. C. 1999, *ApJ*, 523, L165

Caselli, P., Walmsley, C. M., Zucconi, A., Tafalla, M., Dore, L., & Myers P. C. 2002a, *ApJ*, 565, 331

Caselli, P., Walmsley, C. M., Zucconi, A., Tafalla, M., Dore, L., & Myers, P. C. 2002b, *ApJ*, 565, 344

Caselli, P., Benson, P. J., Myers, P. C., & Tafalla, M. 2002c, *ApJ*, 572, 238

Ciolek, G. E. & Basu, S. 2000, *ApJ*, 529, 925

Ciolek, G. E. & Mouschovias, T. C. 1995, *ApJ*, 454, 194

Crapsi, A., Caselli, P., Walmsley, C. M., Tafalla, M., Lee, C. W., Bourke, T. L., & Myers, P. C. 2004, *A&A*, 420, 957

Crutcher, R. M., Nutter, D. J., Ward-Thompson, D., & Kirk, J. M. 2004, *ApJ*, 600, 279

Curry, C. L. & Stahler, S. W. 2001, *ApJ*, 555, 160

Curry, C. L. 2002, *ApJ*, 576, 849

Dalgarno, A. & Lepp, S. 1984, *ApJ*, 287, L47

Dore, L., Caselli, P., Beninati, S., Bourke, T., Myers, P. C., & Cazzoli, G. 2004, *A&A*, 413, 1177

Evans, N. J., II, Rawlings, J. C. M., Shirley, Y., Mundy, L. G. 2001, *ApJ*, 557, 193

Foster, P. N. & Chevalier, R. A. 1993, *ApJ*, 416, 303

Frerking, M. A., Langer, W. D., & Wilson, R. W. 1982, *ApJ*, 262, 590

Galli, D., Walmsley, M., & Gonçalves, J. 2002, *A&A*, 394, 275

Gerlich, D., Herbst, E., & Roueff, E. 2002, *Planet. Space Sci.*, 50, 1275

Gonçalves, J., Galli, D., Walmsley, C. M. 2004, *A&A*, 415, 617

Green, S. 1975, *ApJ*, 201, 366

Harvey, D. W. A., Wilner, D. J., Lada, C. J., Myers, P. C., & Alves, J. F. 2003, *ApJ*, 598, 1112

Hasegawa, T. I. & Herbst, E. 1993, *MNRAS*, 263, 589

Henning, T., Michel, B., & Stognienko, R. 1995, *Planet. Space Sci.*, 43, 1333

Hirota, T., Ikeda, M., & Yamamoto, S. 2003, *ApJ*, 594, 859

Jones, C. E. & Basu, S. 2002, *ApJ*, 569, 280

Keto, E., Rybicki, G. B., Bergin, E. A., & Plume, R. 2004, [astro-ph/0407433]

Kramer, C., Alves, J., Lada, C. J., Lada, E. A., Sievers, A., Ungerechts, H., & Walmsley, C. M. 1999, *A&A*, 342, 257

Kramer, C., Richer, J., Mookerjea, B., Alves, J., & Lada, C. 2003, *A&A*, 399, 1073

Kuiper, T. B. H., Langer, W. D., & Velusamy, T. 1996, *ApJ*, 468, 761

Lacy, J. H., Knacke, R., Geballe, T. R., Tokunaga, A. T. 1994, *ApJ*, 428, L69

Lada, C. J., Bergin, E. A., Alves, J. F., & Huard, T. L. 2003, *ApJ*, 586, 286

Lee, C. W., Myers, P. C., & Tafalla, M. 1999, *ApJ*, 526, 788

Lee, C. W., Myers, P. C., & Tafalla, M. 2001, *ApJS*, 136, 703

Lee, C. W., Myers, P. C., & Plume, R. 2004, *ApJS*, 153, 523

Leger, A. 1983, *A&A*, 123, 271

Li, Z. 1999, *ApJ*, 526, 806

Li, Z., Shematovich, V. I., Wiebe, D. S., & Shustov, B. M. 2002, *ApJ*, 569, 792

Lizano, S. & Shu, F. H. 1989, *ApJ*, 342, 834

Nurmanova, U. A. 1983, *Peremennye Zvezdy*, 21, 777

Maret, S., et al. 2004, *A&A*, 416, 577

Mathis, J. S., Rumpl, W., & Nordsieck, K. H. 1977, *ApJ*, 217, 425

Oliveira, C. M., Hébrard, G., Howk, J. C., Kruk, J. W., Chayer, P., & Moos, H. W. 2003, *ApJ*, 587, 235

Pagani, L. et al. 2003, *A&A*, 406, L59

Press, W. H., Teukolsky, S. A., Vetterling, W. T., & Flannery, B. P. 1988, *Numerical Recipes in C. The art of scientific computing*, (2nd ed.; Cambridge: Cambridge University Press)

Roberts, H. & Millar, T. J. 2000, A&A, 361, 388

Roberts, H., Herbst, E., & Millar, T. J. 2004, A&A, in press

Roueff, E., Tiné, S., Coudert, L. H., Pineau des Forêts, G., Falgarone, E., & Gerin, M. 2000, A&A, 354, L63

Sadlej, J., Rowland, B., Devlin, J. P., & Buch, V. 1995, J. Chem. Phys., 102, 4804

Shematovich, V. I., Wiebe, D. S., Shustov, B. M., & Li, Z. 2003, ApJ, 588, 894

Shirley, Y. L., Evans, N. J., Rawlings, J. M. C., & Gregersen, E. M. 2000, ApJS, 131, 249

Tafalla, M., Myers, P. C., Caselli, P., Walmsley, C. M., & Comito, C. 2002, ApJ, 569, 815

Tiné, S., Roueff, E., Falgarone, E., Gerin, M., & Pineau des Forêts, G. 2000, A&A, 356, 1039

Verhoeve, P., Zwart, E., Versluis, M., Drabbels, M., Ter Meulen, J. J., Meerts, W. L., Dymanus, A., & McLay, D. B. 1990, Review of Scientific Instruments, 61, 1612

Visser, A. E., Richer, J. S., & Chandler, C. J. 2002, AJ, 124, 2756

Walmsley, C. M., Flower, D. R., & Pineau des Forêts, G. 2004, A&A, 418, 1035

Walsh, A. J., & Myers, P. C. 2004, ApJ, accepted

Ward-Thompson, D., Motte, F., & Andre, P. 1999, MNRAS, 305, 143

Wendker, H. J. 1995, A&AS, 109, 177

Wilson, T. L. & Rood, R. 1994, ARA&A, 32, 191

Zucconi, A., Walmsley, C. M., & Galli, D. 2001, A&A, 376, 650

Table 1. Core Sample

core (1)	RA (J2000) (2)	DEC (J2000) (3)	dist (4)	ref (5)	env. (6)	N (7)	1.2-mm (8)	C <sup>18</sup> O (9)
L1498	04 <sup>h</sup> 10 <sup>m</sup> 51 <sup>s</sup> .5	+25°09'58"	140	a	T	25	y (b)	y (b)
L1495	04 <sup>h</sup> 14 <sup>m</sup> 08 <sup>s</sup> .2	+28°08'16"	140	b	T	20	y (b)	y (b)
L1495B	04 <sup>h</sup> 18 <sup>m</sup> 05 <sup>s</sup> .1	+28°22'22"	140	a	T	1	n	n
L1495A-N	04 <sup>h</sup> 18 <sup>m</sup> 31 <sup>s</sup> .8	+28°27'30"	140	a	T	1	n	n
L1495A-S	04 <sup>h</sup> 18 <sup>m</sup> 41 <sup>s</sup> .8	+28°23'50"	140	a	T	1	n	n
L1521F	04 <sup>h</sup> 28 <sup>m</sup> 39 <sup>s</sup> .8	+26°51'35"	140	a	T	89	y (g)	y (g)
L1400K	04 <sup>h</sup> 30 <sup>m</sup> 52 <sup>s</sup> .1	+54°51'55"	140	b	T	20	n	n
L1400A	04 <sup>h</sup> 30 <sup>m</sup> 56 <sup>s</sup> .8	+54°52'36"	140	a	T	1	n	n
TMC2	04 <sup>h</sup> 32 <sup>m</sup> 48 <sup>s</sup> .7	+24°25'12"	140	a	T	1	y (h)	y (h)
TMC1	04 <sup>h</sup> 41 <sup>m</sup> 32 <sup>s</sup> .9	+25°44'44"	140	a	T	1	n	n
TMC1C	04 <sup>h</sup> 41 <sup>m</sup> 38 <sup>s</sup> .8	+25°59'42"	140	c	T	3	n	n
L1507A	04 <sup>h</sup> 42 <sup>m</sup> 38 <sup>s</sup> .6	+29°43'45"	140	a	T	1	n	n
CB23	04 <sup>h</sup> 43 <sup>m</sup> 27 <sup>s</sup> .7	+29°39'11"	140	a	T	1	n	n
L1517B	04 <sup>h</sup> 55 <sup>m</sup> 18 <sup>s</sup> .8	+30°38'04"	140	a	T	21	y (b)	y (b)
L1512	05 <sup>h</sup> 04 <sup>m</sup> 09 <sup>s</sup> .7	+32°43'09"	140	a	T	25	n	n
L1544	05 <sup>h</sup> 04 <sup>m</sup> 15 <sup>s</sup> .1	+25°11'08"	140	a	T	38	y (i)	y (o)
L134A	15 <sup>h</sup> 53 <sup>m</sup> 33 <sup>s</sup> .1	-04°35'26"	165	a	B	1	n	n
L183	15 <sup>h</sup> 54 <sup>m</sup> 06 <sup>s</sup> .4	-02°52'23"	165	a	B	77	y (l)	y (h)
OphD	16 <sup>h</sup> 28 <sup>m</sup> 30 <sup>s</sup> .4	-24°18'29"	165	d	O	78	y (i)	y (p)
L1689A	16 <sup>h</sup> 32 <sup>m</sup> 13 <sup>s</sup> .1	-25°03'43"	165	e	O	1	n	n
L1689B	16 <sup>h</sup> 34 <sup>m</sup> 45 <sup>s</sup> .8	-24°37'50"	165	a	O	1	n	n
L158	16 <sup>h</sup> 47 <sup>m</sup> 23 <sup>s</sup> .2	-13°58'37"	165	a	O	1	n	n
L234E-S	16 <sup>h</sup> 48 <sup>m</sup> 08 <sup>s</sup> .6	-10°57'25"	165	a	O	1	n	n
B68	17 <sup>h</sup> 22 <sup>m</sup> 38 <sup>s</sup> .9	-23°49'46"	125	f	B	1	y (m)	y (f)
L492	18 <sup>h</sup> 15 <sup>m</sup> 46 <sup>s</sup> .1	-03°46'13"	200	a	A	9	y (h)	y (h)
L328	18 <sup>h</sup> 17 <sup>m</sup> 00 <sup>s</sup> .4	-18°01'52"	200	d	B	4	y (d)	y (p)
L429	18 <sup>h</sup> 17 <sup>m</sup> 06 <sup>s</sup> .4	-08°14'00"	200	a	A	68	y (d)	y (p)
GF5	18 <sup>h</sup> 39 <sup>m</sup> 16 <sup>s</sup> .4	-06°38'15"	200	d	A	1	n	n
L694-2	19 <sup>h</sup> 41 <sup>m</sup> 04 <sup>s</sup> .5	+10°57'02"	250	a	...	96	y (n)	y (h)
L1197	22 <sup>h</sup> 37 <sup>m</sup> 02 <sup>s</sup> .3	+58°57'21"	...	a	...	5	n	n
CB246	23 <sup>h</sup> 56 <sup>m</sup> 49 <sup>s</sup> .2	+58°34'29"	140	a	B	3	n	n

Note. — Col (1) most common core name; col. (2) and (3) reference position in J2000; col. (4) distance; col. (5) references for the position and distance, see below for coding; col. (6) Star forming environment: T: Taurus molecular cloud; O: Ophiucus molecular cloud; B: Bok globules; A: Aquila rift; col. (7) number of observed positions in both  $\text{N}_2\text{H}^+$  and  $\text{N}_2\text{D}^+$ ; col. (8) availability of a 1.2-mm continuum map and reference to it, coding below; col. (9) availability of a  $\text{C}^{18}\text{O}$  map and reference to it, coding below.

References. — a: Lee et al. (2001); b: Tafalla et al. (2002); c: Caselli et al. (2002c); d: Bacmann et al. (2000); e: Shirley et al. (2000); f: Bergin et al. (2002); g: Crapsi et al. (2004); h: this work; i: Ward-Thompson et al. (1999); l: Pagani et al. (2003); m: Bianchi et al. (2003); n: Tafalla et al. (2004); o: Caselli et al. (1999); p: Bacmann et al. (2001).

Table 2. Telescope settings and parameters.

line (1)	frequency (2)	HPBW (3)	$F_{throw}$ (4)	$T_{SYS}$ (5)	$\Delta v_{res}$ (6)
$N_2H^+(1-0)$	93.1737725	26	7.5	200	0.063
$N_2H^+(3-2)$	279.511863	9	14.3	2000	0.042
$N_2D^+(2-1)$	154.217137	16	7.5	400	0.038
$N_2D^+(3-2)$	231.321966	10	14.3	900	0.050
$C^{18}O(1-0)$	109.782173	22	...	170	0.026
$C^{18}O(2-1)$	219.560357	11	...	450	0.033

Note. — Col. (2) line rest frequency (GHz); Col. (3) Half Power Beam Width ('') Col. (4) Freq. Throw (kHz); Col. (5) System Temperature (K); Col. (6) Channel Spacing ( $\text{km s}^{-1}$ )

Table 3. Observed line integrated intensities at  $\text{N}_2\text{D}^+$  peak.

core	RA off "	DEC off "	$I(\text{N}_2\text{H}^+(1-0))$ K km s $^{-1}$	$I(\text{N}_2\text{H}^+(3-2))$ K km s $^{-1}$	$I(\text{N}_2\text{D}^+(2-1))$ K km s $^{-1}$	$I(\text{N}_2\text{D}^+(3-2))$ K km s $^{-1}$
L1498	0	0	$2.27 \pm 0.01$	$0.11 \pm 0.02$	$0.12 \pm 0.02$	$< 0.01$
L1495	40	40	$3.18 \pm 0.03$	$0.24 \pm 0.04$	$0.23 \pm 0.05$	$0.08 \pm 0.02$
L1495B	0	0	$1.35 \pm 0.05$	$< 0.09$	$0.14 \pm 0.04$	$0.30 \pm 0.09$
L1495A-N	0	0	$3.46 \pm 0.05$	$< 0.09$	$0.18 \pm 0.02$	$< 0.09$
L1495A-S	0	0	$1.08 \pm 0.06$	$< 0.12$	$0.15 \pm 0.04$	$< 0.11$
L1521F	-10	0	$5.86 \pm 0.02$	$0.74 \pm 0.04$	$0.97 \pm 0.02$	$0.29 \pm 0.01$
L1400K	-20	-40	$1.39 \pm 0.02$	$0.10 \pm 0.04$	$< 0.04$	$< 0.02$
L1400A	0	0	$1.48 \pm 0.04$	$0.25 \pm 0.12$	$0.08 \pm 0.02$	$0.13 \pm 0.07$
TMC2	0	40	$3.48 \pm 0.03$	$0.32 \pm 0.11$	$0.66 \pm 0.04$	$0.17 \pm 0.05$
TMC1	0	0	$3.51 \pm 0.06$	$0.35 \pm 0.11$	$0.20 \pm 0.03$	$< 0.10$
TMC1C	0	40	$1.87 \pm 0.03$	$< 0.19$	$0.24 \pm 0.04$	$0.08 \pm 0.06$
L1507A	0	0	$1.78 \pm 0.05$	$0.21 \pm 0.12$	$0.15 \pm 0.03$	$0.15 \pm 0.07$
CB23	0	0	$2.22 \pm 0.06$	$0.20 \pm 0.14$	$0.21 \pm 0.04$	$0.37 \pm 0.10$
L1517B	-15	-15	$2.57 \pm 0.01$	$0.11 \pm 0.02$	$0.26 \pm 0.02$	$< 0.01$
L1512	0	0	$2.11 \pm 0.02$	$< 0.05$	$0.17 \pm 0.03$	$< 0.02$
L1544	20	-20	$5.46 \pm 0.04$	$0.56 \pm 0.09$	$2.23 \pm 0.05$	$0.55 \pm 0.03$
L134A	0	0	$1.13 \pm 0.03$	$< 0.25$	$< 0.04$	$< 0.07$
L183	30	0	$4.20 \pm 0.01$	$0.56 \pm 0.04$	$1.63 \pm 0.02$	$0.48 \pm 0.01$
OphD	-20	-50	$3.71 \pm 0.02$	$0.39 \pm 0.05$	$1.75 \pm 0.02$	$0.59 \pm 0.02$
L1689A	0	0	$0.15 \pm 0.07$	$< 0.13$	$< 0.05$	$< 0.06$
L1689B	0	0	$1.27 \pm 0.05$	$< 0.13$	$0.09 \pm 0.04$	$0.12 \pm 0.06$
L158	0	0	$0.61 \pm 0.05$	$< 0.11$	$< 0.04$	$< 0.05$
L234E-S	0	0	$2.06 \pm 0.07$	$0.40 \pm 0.26$	$0.26 \pm 0.04$	$< 0.32$
B68	0	0	$2.37 \pm 0.01$	$0.17 \pm 0.02$	$0.13 \pm 0.03$	$< 0.03$
L492	20	20	$3.95 \pm 0.02$	$< 0.10$	$0.30 \pm 0.02$	$< 0.04$
L328	0	0	$4.46 \pm 0.03$	$0.42 \pm 0.09$	$0.38 \pm 0.03$	$0.19 \pm 0.04$
L429	-20	20	$6.11 \pm 0.02$	$0.57 \pm 0.05$	$2.03 \pm 0.02$	$0.62 \pm 0.02$
GF5	0	0	$0.39 \pm 0.05$	$< 0.07$	$< 0.04$	$< 0.10$
L694-2	0	0	$5.13 \pm 0.01$	$0.36 \pm 0.02$	$1.35 \pm 0.02$	$0.37 \pm 0.01$
L1197	0	0	$2.15 \pm 0.04$	$< 0.16$	$0.18 \pm 0.06$	$< 0.05$
CB246	-60	-20	$2.91 \pm 0.03$	$< 0.07$	$0.11 \pm 0.04$	$0.22 \pm 0.06$

Note. — Offsets are referred to the positions in Table 1. Temperatures are in main beam temperature scale. Calibration errors were not included in the error estimate. Upper limits assume the line-width of  $\text{N}_2\text{H}^+(1-0)$  where available or  $0.17 \text{ km s}^{-1}$  the smallest line-width observed in our sample.

Table 4. Results of the hyperfine structure fitting on the  $\text{N}_2\text{H}^+(1-0)$  and  $\text{N}_2\text{D}^+(2-1)$  spectra at the peak position of each core.

core	$\text{N}_2\text{H}^+(1-0)$				$\text{N}_2\text{D}^+(2-1)$			
	$V_{LSR}$ km s $^{-1}$	$\Delta V$ km s $^{-1}$	$\tau$	$T_{EX}$ K	$V_{LSR}$ km s $^{-1}$	$\Delta V$ km s $^{-1}$	$\tau$	$T_{EX}$ K
L1498	7.822 $\pm$ 0.001	0.185 $\pm$ 0.001	11.5 $\pm$ 0.3	4.5 $\pm$ 0.1	7.778 $\pm$ 0.010	0.176 $\pm$ 0.029	0.1	4.5
L1495	6.807 $\pm$ 0.001	0.237 $\pm$ 0.003	9.6 $\pm$ 0.6	4.8 $\pm$ 0.2	6.755 $\pm$ 0.025	0.290 $\pm$ 0.061	0.1	4.8
L1495B	6.633 $\pm$ 0.008	0.390 $\pm$ 0.018	0.1	4.8	6.683 $\pm$ 0.065	0.500 $\pm$ 0.216	0.1	4.8
L1495A-N	7.296 $\pm$ 0.003	0.327 $\pm$ 0.007	7.6 $\pm$ 0.9	4.7 $\pm$ 0.3	7.237 $\pm$ 0.013	0.244 $\pm$ 0.035	0.1	4.7
L1495A-S	7.294 $\pm$ 0.007	0.214 $\pm$ 0.015	21.3 $\pm$ 5.3	4.4 $\pm$ 0.4	7.264 $\pm$ 0.024	0.284 $\pm$ 0.059	0.1	4.4
L1521F	6.472 $\pm$ 0.001	0.299 $\pm$ 0.001	17.9 $\pm$ 0.3	4.9 $\pm$ 0.1	6.505 $\pm$ 0.004	0.268 $\pm$ 0.010	2.2 $\pm$ 0.4	4.6 $\pm$ 0.3
L1400K	3.196 $\pm$ 0.002	0.231 $\pm$ 0.005	6.5 $\pm$ 0.8	4.4 $\pm$ 0.5	...	...	...	...
L1400A	3.355 $\pm$ 0.002	0.191 $\pm$ 0.006	7.7 $\pm$ 1.2	4.4 $\pm$ 0.6	3.250 $\pm$ 0.036	0.175 $\pm$ 0.061	0.1	4.4
TMC2	6.193 $\pm$ 0.001	0.210 $\pm$ 0.002	8.7 $\pm$ 0.4	5.1 $\pm$ 0.2	6.157 $\pm$ 0.006	0.167 $\pm$ 0.015	4.5 $\pm$ 1.1	5.0 $\pm$ 0.3
TMC1	5.856 $\pm$ 0.003	0.269 $\pm$ 0.007	11.1 $\pm$ 1.2	4.6 $\pm$ 0.3	5.870 $\pm$ 0.040	0.409 $\pm$ 0.113	0.1	4.6
TMC1C	5.196 $\pm$ 0.003	0.212 $\pm$ 0.006	18.4 $\pm$ 2.2	4.4 $\pm$ 0.5	5.193 $\pm$ 0.009	0.132 $\pm$ 0.017	0.1	4.4
L1507A	6.163 $\pm$ 0.004	0.220 $\pm$ 0.009	12.2 $\pm$ 2.1	4.4 $\pm$ 0.6	6.159 $\pm$ 0.030	0.254 $\pm$ 0.071	0.1	4.4
CB23	6.015 $\pm$ 0.002	0.166 $\pm$ 0.006	14.6 $\pm$ 2.2	4.4 $\pm$ 0.3	5.985 $\pm$ 0.027	0.233 $\pm$ 0.075	0.1	4.4
L1517B	5.835 $\pm$ 0.001	0.215 $\pm$ 0.001	8.8 $\pm$ 0.2	4.7 $\pm$ 0.1	5.796 $\pm$ 0.008	0.218 $\pm$ 0.017	0.1	4.7
L1512	7.121 $\pm$ 0.001	0.174 $\pm$ 0.001	7.3 $\pm$ 0.4	5.0 $\pm$ 0.2	7.091 $\pm$ 0.018	0.274 $\pm$ 0.076	0.1	4.8
L1544	7.143 $\pm$ 0.002	0.315 $\pm$ 0.004	12.6 $\pm$ 0.7	5.0 $\pm$ 0.2	7.181 $\pm$ 0.004	0.289 $\pm$ 0.008	5.2 $\pm$ 0.4	4.8 $\pm$ 0.2
L134A	2.665 $\pm$ 0.002	0.215 $\pm$ 0.007	4.3 $\pm$ 1.0	4.4 $\pm$ 0.6	...	...	...	...
L183	2.413 $\pm$ 0.001	0.211 $\pm$ 0.001	20.3 $\pm$ 0.2	4.8 $\pm$ 0.1	2.459 $\pm$ 0.001	0.214 $\pm$ 0.002	4.7 $\pm$ 0.2	4.9 $\pm$ 0.1
OphD	3.478 $\pm$ 0.001	0.223 $\pm$ 0.001	4.4 $\pm$ 0.1	7.1 $\pm$ 0.2	3.515 $\pm$ 0.001	0.204 $\pm$ 0.003	4.3 $\pm$ 0.2	5.3 $\pm$ 0.2
L158	3.942 $\pm$ 0.007	0.229 $\pm$ 0.014	0.1	4.8	...	...	...	...
L1689B	3.481 $\pm$ 0.005	0.262 $\pm$ 0.011	0.1	4.8	3.642 $\pm$ 0.058	0.373 $\pm$ 0.148	0.1	4.8
L234E-S	3.164 $\pm$ 0.003	0.198 $\pm$ 0.008	6.9 $\pm$ 1.5	4.7 $\pm$ 0.5	3.286 $\pm$ 0.015	0.182 $\pm$ 0.055	0.1	4.7
B68	3.364 $\pm$ 0.001	0.176 $\pm$ 0.001	26.2 $\pm$ 1.0	4.5 $\pm$ 0.5	3.372 $\pm$ 0.016	0.124 $\pm$ 0.036	0.1	4.5
L492	7.701 $\pm$ 0.001	0.263 $\pm$ 0.001	11.8 $\pm$ 0.2	4.8 $\pm$ 0.1	7.726 $\pm$ 0.008	0.222 $\pm$ 0.022	2.6 $\pm$ 0.8	4.4 $\pm$ 0.3
L328	6.707 $\pm$ 0.002	0.438 $\pm$ 0.005	8.1 $\pm$ 0.5	4.6 $\pm$ 0.2	6.797 $\pm$ 0.012	0.419 $\pm$ 0.028	0.1	4.6
L429	6.719 $\pm$ 0.001	0.394 $\pm$ 0.001	12.3 $\pm$ 0.1	4.9 $\pm$ 0.1	6.705 $\pm$ 0.002	0.360 $\pm$ 0.005	4.3 $\pm$ 0.2	4.4 $\pm$ 0.1
L694-2	9.574 $\pm$ 0.001	0.266 $\pm$ 0.001	13.9 $\pm$ 0.1	5.2 $\pm$ 0.1	9.567 $\pm$ 0.002	0.244 $\pm$ 0.004	5.5 $\pm$ 0.2	4.1 $\pm$ 0.1
L1197	-3.147 $\pm$ 0.002	0.249 $\pm$ 0.006	6.5 $\pm$ 0.9	4.5 $\pm$ 0.3	-3.020 $\pm$ 0.016	0.180 $\pm$ 0.093	0.1	4.5
CB246	-0.830 $\pm$ 0.001	0.245 $\pm$ 0.003	10.3 $\pm$ 0.7	4.5 $\pm$ 0.2	-0.730 $\pm$ 0.025	0.126 $\pm$ 0.039	0.1	4.5

Note. — The hyperfine fitting model assumes constant  $T_{EX}$  and homogenous abundance and do not consider velocity gradients effects along the line of sight. L1689A and GF5 spectra were not fitted because of poor S/N.

Table 5. Results of the hyperfine structure fitting on the  $\text{N}_2\text{H}^+(3-2)$  and  $\text{N}_2\text{D}^+(3-2)$  spectra at the peak position of each core. Only the fits to high S/N ( $> 5$ ) spectra are reported.

core	$\text{N}_2\text{H}^+(3-2)$			$\text{N}_2\text{D}^+(3-2)$		
	$V_{LSR}$ km s $^{-1}$	$\Delta V$ km s $^{-1}$	$\tau$	$V_{LSR}$ km s $^{-1}$	$\Delta V$ km s $^{-1}$	$\tau$
L1498	$7.786 \pm 0.015$	$0.169 \pm 0.040$	$< 0.1$	...	...	...
L1495	$6.811 \pm 0.030$	$0.288 \pm 0.052$	$< 0.1$	...	...	...
L1521F	$6.391 \pm 0.010$	$0.172 \pm 0.021$	$6.2 \pm 1.5$	$6.507 \pm 0.006$	$0.222 \pm 0.025$	$1.2 \pm 0.9$
L1517B	$5.816 \pm 0.030$	$0.219 \pm 0.130$	$< 0.2$	...	...	...
L1544	$7.138 \pm 0.018$	$0.193 \pm 0.080$	$< 0.1$	$7.208 \pm 0.012$	$0.342 \pm 0.026$	$< 0.1$
L183	$2.412 \pm 0.012$	$0.220 \pm 0.036$	$3.5 \pm 1.6$	$2.445 \pm 0.003$	$0.205 \pm 0.012$	$1.2 \pm 0.4$
OphD	$3.466 \pm 0.011$	$0.131 \pm 0.019$	$6.7 \pm 2.2$	$3.503 \pm 0.004$	$0.196 \pm 0.013$	$2.6 \pm 0.6$
B68	$3.370 \pm 0.017$	$0.231 \pm 0.022$	$0.8 \pm 0.4$	...	...	...
L429	$6.673 \pm 0.029$	$0.373 \pm 0.037$	$2.7 \pm 0.4$	$6.696 \pm 0.009$	$0.262 \pm 0.020$	$5.2 \pm 0.9$
L694-2	$9.532 \pm 0.014$	$0.308 \pm 0.060$	$1.7 \pm 1.4$	$9.560 \pm 0.005$	$0.242 \pm 0.016$	$1.5 \pm 0.5$

Table 6. Integrated intensities and results of the gaussian fitting of the  $\text{C}^{18}\text{O}(1-0)$  and  $(2-1)$  spectra towards the peak position for the four cores newly observed.

core	$\text{C}^{18}\text{O}(1-0)$			$\text{C}^{18}\text{O}(2-1)$		
	$I(\text{C}^{18}\text{O}(1-0))$ K km s $^{-1}$	$V_{LSR}$ km s $^{-1}$	$\Delta V$ km s $^{-1}$	$I(\text{C}^{18}\text{O}(2-1))$ K km s $^{-1}$	$V_{LSR}$ km s $^{-1}$	$\Delta V$ km s $^{-1}$
L1521F	$1.80 \pm 0.06$	$6.458 \pm 0.006$	$0.438 \pm 0.014$	$1.80 \pm 0.15$	$6.427 \pm 0.015$	$0.447 \pm 0.034$
TMC2	$1.05 \pm 0.04$	$6.313 \pm 0.007$	$0.401 \pm 0.014$	$1.09 \pm 0.07$	$6.229 \pm 0.010$	$0.392 \pm 0.023$
L183	$1.89 \pm 0.04$	$2.518 \pm 0.006$	$0.545 \pm 0.016$	$2.14 \pm 0.06$	$2.556 \pm 0.008$	$0.579 \pm 0.019$
L492	$0.76 \pm 0.04$	$7.786 \pm 0.017$	$0.651 \pm 0.042$	$0.58 \pm 0.05$	$7.786 \pm 0.022$	$0.529 \pm 0.055$
L694-2	$1.21 \pm 0.04$	$9.574 \pm 0.007$	$0.433 \pm 0.015$	$1.01 \pm 0.04$	$9.574 \pm 0.006$	$0.415 \pm 0.015$

Table 7.  $\text{N}_2\text{H}^+$  and  $\text{N}_2\text{D}^+$  column densities and relative ratio towards the  $\text{N}_2\text{D}^+(2-1)$  integrated intensity peak.

core	$\text{N}(\text{N}_2\text{H}^+)$ $10^{12} \text{ cm}^{-2}$	$\text{N}(\text{N}_2\text{D}^+)$ $10^{11} \text{ cm}^{-2}$	$\text{N}(\text{N}_2\text{D}^+)/\text{N}(\text{N}_2\text{H}^+)$
L1498	$7.1 \pm 0.7$	$2.7 \pm 0.6$	$0.04 \pm 0.01$
L1495	$8.8 \pm 1.0$	$4.2 \pm 1.1$	$0.05 \pm 0.01$
L1495B	$2.8 \pm 0.8$	$2.7 \pm 0.8$	$0.10 \pm 0.04$
L1495A-N	$9.6 \pm 1.2$	$3.6 \pm 0.7$	$0.04 \pm 0.01$
L1495A-S	$4.6 \pm 1.0$	$3.4 \pm 1.0$	$0.08 \pm 0.03$
L1521F	$19.3 \pm 1.9$	$20.0 \pm 3.0$	$0.10 \pm 0.02$
L1400K	$3.6 \pm 0.5$	$<0.8$	$<0.02$
L1400A	$3.6 \pm 0.7$	$1.8 \pm 0.6$	$0.05 \pm 0.02$
TMC2	$9.9 \pm 1.1$	$11.3 \pm 1.8$	$0.11 \pm 0.02$
TMC1	$9.6 \pm 1.3$	$4.1 \pm 0.9$	$0.04 \pm 0.01$
TMC1C	$8.0 \pm 0.9$	$5.5 \pm 1.3$	$0.07 \pm 0.02$
L1507A	$6.9 \pm 0.9$	$3.5 \pm 0.9$	$0.05 \pm 0.01$
CB23	$7.0 \pm 1.2$	$4.8 \pm 1.1$	$0.07 \pm 0.02$
L1517B	$7.9 \pm 0.8$	$5.1 \pm 0.8$	$0.06 \pm 0.01$
L1512	$5.8 \pm 0.6$	$3.1 \pm 0.6$	$0.05 \pm 0.01$
L1544 <sup>a</sup>	$18.3 \pm 1.9$	$42.5 \pm 6.4$	$0.23 \pm 0.04$
L134A	$2.5 \pm 0.5$	$<0.9$	$<0.04$
L183	$13.7 \pm 1.4$	$29.9 \pm 4.5$	$0.22 \pm 0.04$
OphD	$6.3 \pm 0.7$	$27.3 \pm 4.1$	$0.44 \pm 0.08$
L158	$1.0 \pm 0.1$	$<0.7$	$<0.08$
L1689B	$2.0 \pm 0.2$	$1.7 \pm 0.8$	$0.09 \pm 0.04$
L234E-S	$5.9 \pm 1.1$	$5.0 \pm 1.1$	$0.08 \pm 0.02$
B68	$9.7 \pm 1.0$	$2.7 \pm 0.7$	$0.03 \pm 0.01$
L492	$14.4 \pm 1.5$	$6.9 \pm 1.1$	$0.05 \pm 0.01$
L328	$11.6 \pm 1.3$	$7.9 \pm 1.3$	$0.07 \pm 0.01$
L429	$16.7 \pm 1.7$	$45.9 \pm 6.9$	$0.28 \pm 0.05$
L694-2	$14.6 \pm 1.5$	$37.6 \pm 5.7$	$0.26 \pm 0.05$
L1197	$5.7 \pm 0.9$	$4.0 \pm 1.5$	$0.07 \pm 0.03$
CB246	$8.8 \pm 1.0$	$2.4 \pm 0.9$	$0.03 \pm 0.01$

<sup>a</sup>The difference in the L1544  $N(N_2D^+)/N(N_2H^+)$  given by Caselli et al. (2002b) (0.26) and here (0.23) is due to the different approximation used. They evaluated the column density from all the seven hyperfine components correcting for the high optical depth (see their eq. A1) while here we used the optically thin approximation applied on the weakest component only.

Table 8.  $\text{H}_2$  volume density and  $\text{N}_2\text{H}^+ - \text{N}_2\text{D}^+$  column densities derived in the LVG approximation.

core	$\text{N}_2\text{H}^+$		$\text{N}_2\text{D}^+$	
	$n(\text{H}_2)$ $10^5 \text{ cm}^{-3}$	$N(\text{N}_2\text{H}^+)$ $10^{13} \text{ cm}^{-2}$	$n(\text{H}_2)$ $10^5 \text{ cm}^{-3}$	$N(\text{N}_2\text{D}^+)$ $10^{12} \text{ cm}^{-2}$
L1521F	1.3	3.4	4.5	1.6
TMC2	1.7	1.0	1.5	1.5
L1544	1.5	2.8	2.8	4.6
L183	1.0	2.0	3.5	2.8
OphD	3.2	0.6	4.0	2.6
B68	0.6	1.2	...	...
L429	1.6	3.1	4.3	4.9
L694-2	1.1	2.1	2.2	3.3

Note. — Errors in the LVG determinations are estimated around 30% from comparisons with CTEX determinations.

Table 9.  $H_2$  densities, integrated CO depletion factor, flattened radius, aspect ratios and  $N_2H^+(1-0)$  skewness.

core	$N(H_2)$ $10^{22} \text{ cm}^{-2}$	$n(H_2)$ $10^5 \text{ cm}^{-3}$	$f_D(\text{CO})^a$	$r_{70}$ $10^3 \text{ AU}$	aspect ratio 70% contour	aspect ratio 50% contour	$N_2H^+(1-0)$ skewness <sup>b</sup>
L1498	$3.2 \pm 1.0$	$1.0 \pm 0.7$	$7.5 \pm 2.5$	$6.6 \pm 0.7$	$1.6 \pm 0.3$	$1.5 \pm 0.3$	$-0.01 \pm 0.05$
L1495	$3.1 \pm 1.0$	$1.1 \pm 0.7$	$7 \pm 2.4$	$4.7 \pm 0.6$	$2.0 \pm 0.4$	$1.9 \pm 0.4$	$0.10 \pm 0.05$
L1521F	$13.5 \pm 2.2$	$11.0 \pm 1.8$	$15 \pm 3.6$	$3.4 \pm 0.5$	$1.2 \pm 0.1$	$1.6 \pm 0.2$	$0.19 \pm 0.06$
TMC2	$6.0 \pm 1.2$	$3.0 \pm 0.8$	$13 \pm 3.3$	$5.2 \pm 0.6$	$1.2 \pm 0.4$	$1.1 \pm 0.3$	$-0.01 \pm 0.05$
L1517B	$3.7 \pm 1.0$	$2.2 \pm 0.8$	$9.5 \pm 2.8$	$4.0 \pm 0.5$	$1.4 \pm 0.1$	$1.2 \pm 0.1$	$-0.08 \pm 0.05$
L1544	$9.4 \pm 1.6$	$14.0 \pm 2.2$	$14 \pm 3.4$	$3.2 \pm 0.4$	$1.6 \pm 0.2$	$1.9 \pm 0.2$	$0.40 \pm 0.09$
L183	$10.0 \pm 1.7$	$10.0 \pm 1.7$	$12 \pm 3.1$	$4.8 \pm 0.6$	$1.8 \pm 0.2$	$2.5 \pm 0.2$	$0.09 \pm 0.05$
OphD	$8.2 \pm 1.5$	$8.5 \pm 1.5$	$14 \pm 3.4$	$6.1 \pm 0.7$	$2.1 \pm 0.4$	$1.9 \pm 0.4$	$0.54 \pm 0.12$
B68	$1.4 \pm 0.3$	$0.8 \pm 0.7$	$3.4 \pm 2.1$	$3.7 \pm 0.9$	$1.3 \pm 0.3$	$1.3 \pm 0.3$	$-0.09 \pm 0.05$
L492	$4.4 \pm 1.1$	$2.1 \pm 0.8$	$8 \pm 2.6$	$7.8 \pm 0.8$	$1.5 \pm 0.2$	$2.0 \pm 0.2$	$0.25 \pm 0.07$
L328	$5.7 \pm 1.2$	$1.8 \pm 0.7$	$8.5 \pm 2.6$	$3.7 \pm 0.5$	$1.1 \pm 0.2$	$1.2 \pm 0.2$	$-0.02 \pm 0.08$
L429	$8.8 \pm 1.6$	$6.0 \pm 1.1$	$15.5 \pm 3.7$	$3.6 \pm 0.5$	$1.4 \pm 0.2$	$2.1 \pm 0.3$	$-0.20 \pm 0.10$
L694-2	$7.8 \pm 1.4$	$9.0 \pm 1.5$	$11 \pm 3.0$	$5.5 \pm 0.6$	$1.3 \pm 0.1$	$1.4 \pm 0.1$	$0.22 \pm 0.07$

Note. — For reference to the literature data see text.

<sup>a</sup>The CO depletion factor in L1689B is  $4.5 \pm 2.2$ .

<sup>b</sup> $N_2H^+(1-0)$  skewness was measured also in: L1495A-N ( $-0.04 \pm 0.05$ ); L1400K ( $-0.42 \pm 0.10$ ); TMC1 ( $-0.13 \pm 0.06$ ); TMC1C ( $0.43 \pm 0.10$ ); L1512 ( $0.02 \pm 0.05$ ); L234E-S ( $-0.25 \pm 0.07$ ); L1197 ( $0.08 \pm 0.11$ ); CB246 ( $0.02 \pm 0.05$ ).

Table 10. Chemical and kinematical evolution “probes” in the 12 cores with full data set ( $\text{N}_2\text{H}^+$ ,  $\text{N}_2\text{D}^+$ ,  $\text{C}^{18}\text{O}$  and 1.2-mm emission).

core	L1544	L1521F	L694-2	L429	L183	OphD	TMC2	L492	L328	L1495	L1517B	L1498
$\text{N}(\text{N}_2\text{D}^+) > 1.0 \times 10^{12} \text{ cm}^{-2}$	1	1	1	1	1	1	1	0	0	0	0	0
$\text{N}(\text{N}_2\text{H}^+) > 8.5 \times 10^{12} \text{ cm}^{-2}$	1	1	1	1	1	0	1	1	1	1	1	0
$\frac{[\text{N}_2\text{D}^+]}{[\text{N}_2\text{H}^+]} > 0.10$	1	1	1	1	1	1	1	0	0	0	0	0
$f_{\text{D}}(\text{CO}) > 10.2$	1	1	1	1	1	1	1	0	0	0	0	0
$n(\text{H}_2) > 5.1 \times 10^5 \text{ cm}^{-3}$	1	1	1	1	1	1	0	0	0	0	0	0
$\Delta V_{\text{N}_2\text{H}^+} > 0.25 \text{ km s}^{-1}$	1	1	1	1	0	0	0	1	1	0	0	0
infall asym. ( $skewness > 0$ )	1	1	1	0	1	1	0	1	0	1	0	0
$r_{70} < 4800 \text{ AU}$	1	1	0	1	1	0	0	0	1	1	1	0
total	8	8	7	7	7	5	4	3	3	3	2	0

Note. — For each value, but the skewness, the thresholds are given by the arithmetic mean value for the sample.

Table 11.  $\text{N}_2\text{H}^+$ ,  $\text{N}_2\text{D}^+$  and 1.2-mm maps full width at half maximum.

core	1.2mm	$\text{N}_2\text{H}^+(1-0)$	$\text{N}_2\text{H}^+(3-2)$	$\text{N}_2\text{D}^+(2-1)$	$\text{N}_2\text{D}^+(3-2)$
L183	$185'' \times 67''$	$217'' \times 92''$	...	$93'' \times 72''$	...
OphD	$129'' \times 70''$	$170'' \times 70''$	...	$93'' \times 62''$	$67'' \times 65''$
L492	$180'' \times 100''$	$98'' \times 78''$	...	...	...
L429	$102'' \times 53''$	$91'' \times 78''$	$72'' \times 53''$	$60'' \times 56''$	$43'' \times 41''$
L694-2	$77'' \times 55''$	$85'' \times 67''$	...	$68'' \times 60''$	...

Table 12. Global and local velocity gradients from  $\text{N}_2\text{H}^+(1-0)$  maps.

core	$\mathcal{G}$ km s <sup>-1</sup> pc <sup>-1</sup>	$\Theta^a$ °	$\langle \mathcal{G}_l \rangle^b$ km s <sup>-1</sup> pc <sup>-1</sup>
L183	1.4±0.1	-49±1	1.5±0.7
OphD	1.6±0.1	-119±1	1.6±1.0
L694-2	0.7±0.1	-18±1	0.8±0.3
L429	0.4±0.1	-33±2	1.9±1.1
L492	0.2±0.1	83±2	1.5±0.8

<sup>a</sup>Direction of increasing velocity, measured East of North.

<sup>b</sup>Mean values of the magnitude of local gradients and corresponding standard error.

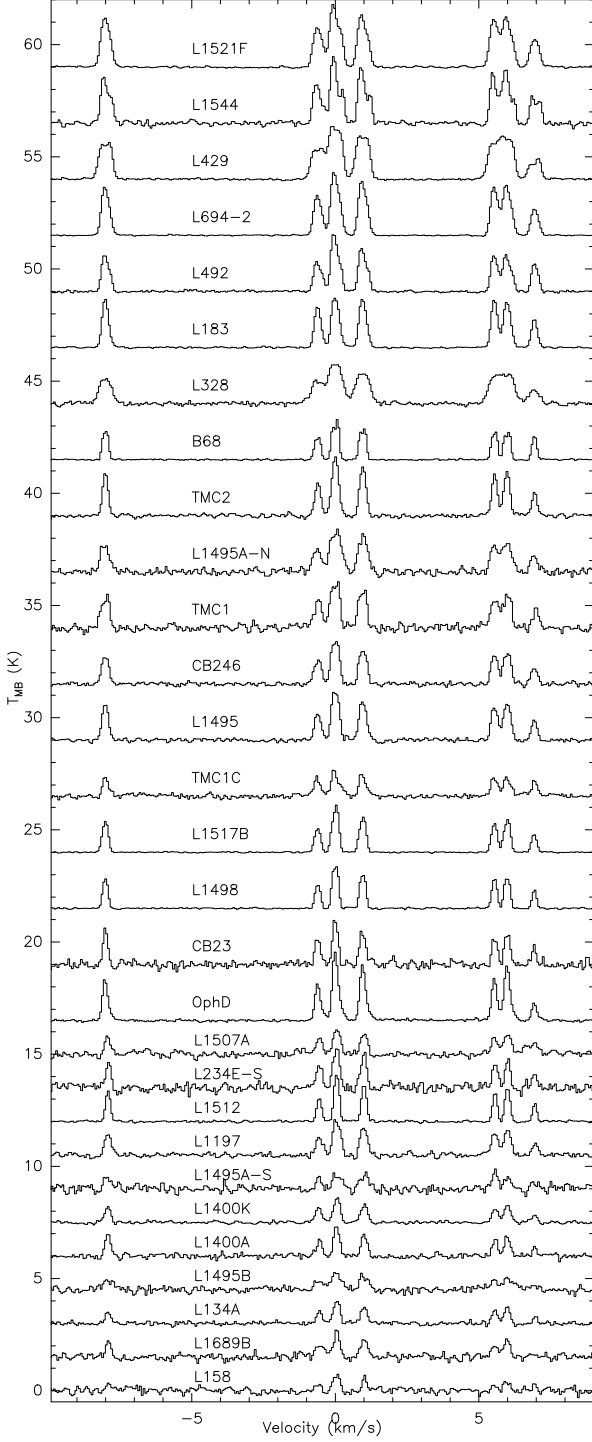


Fig. 1.—  $\text{N}_2\text{H}^+(1-0)$  spectra at peak sorted by decreasing  $\text{N}_2\text{H}^+$  column density. The 2 sources with no detection (L1689A, GF5) were omitted.

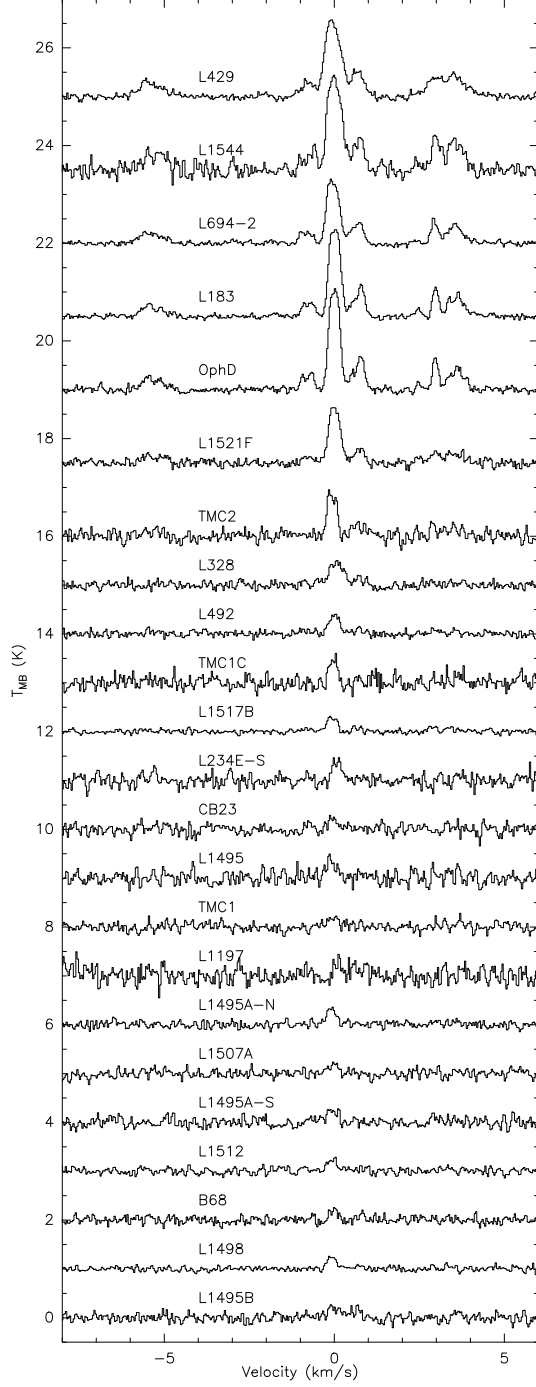


Fig. 2.—  $\text{N}_2\text{D}^+(2-1)$  spectra at peak sorted by decreasing  $\text{N}_2\text{D}^+$  column density. 8 sources with marginal or no detection were omitted (L1400K, L1400A, L134A, L1689A, L1689B, L158, GF5, CB246).

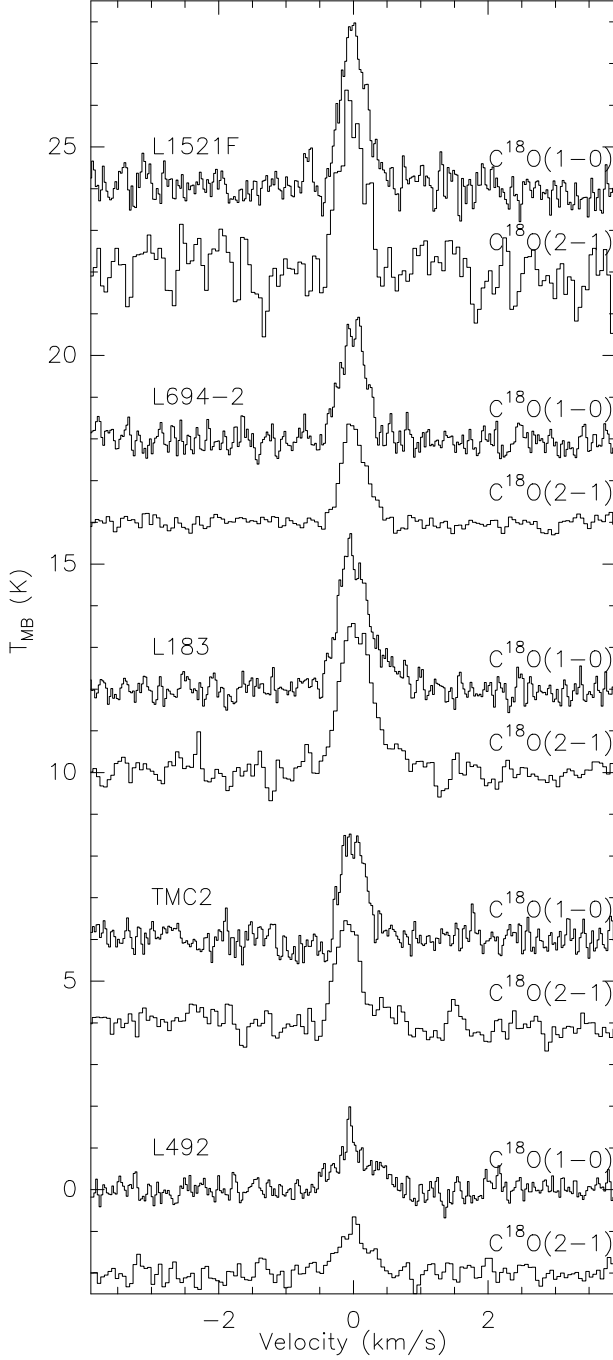


Fig. 3.—  $\text{C}^{18}\text{O}(1-0)$  and  $(2-1)$  spectra towards L1521F, L694-2, L183, TMC2 and L492. The shown spectra are the arithmetic means of all the observations in the  $10''$  strip centered around the peak position and going parallel to the Right Ascension direction.

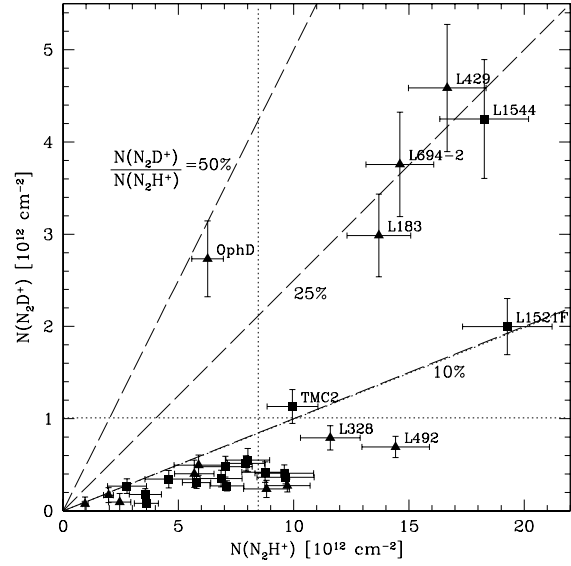


Fig. 4.—  $\text{N}_2\text{H}^+$  column density vs.  $\text{N}_2\text{D}^+$  column density at  $\text{N}_2\text{D}^+$  peak position. Deuterium fractionation can be read from the radial dashed lines (corresponding to  $\text{N}(\text{N}_2\text{D}^+)/\text{N}(\text{N}_2\text{H}^+)$  0.1, 0.25 and 0.5). Dotted lines are the arithmetic means of the distributions. Cores belonging to the Taurus Molecular Cloud are marked with a square.

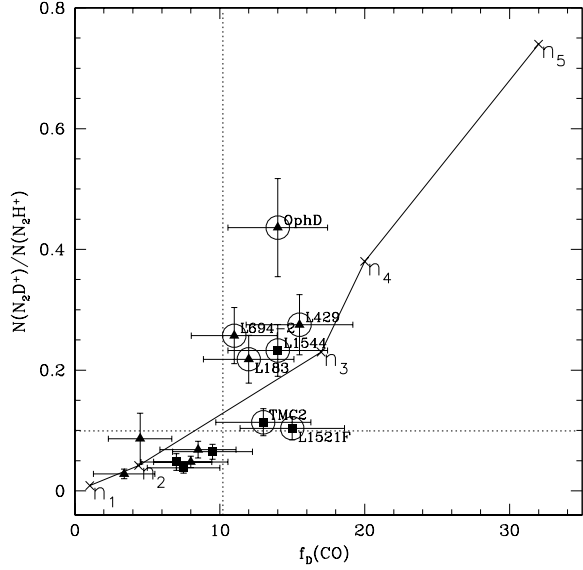


Fig. 5.— Deuterium fractionation vs. integrated CO depletion factor at the  $\text{N}_2\text{D}^+$  peak position. Depletion factors values were taken from literature and from present data (see Section 4.2 for references). The solid line connects the predictions of chemical models of spherically symmetric dense cores with various degrees of central concentrations (from central densities of  $4.4 \times 10^4 \text{ cm}^{-3}$  in model  $n_1$  to  $4.4 \times 10^8 \text{ cm}^{-3}$  in model  $n_5$ ), roughly simulating (in spherical symmetry) the evolutionary sequence of contracting disk-like clouds in the Ciolek & Basu (2000) model (see text). Dotted lines are the arithmetic means of the distributions. Cores belonging to the Taurus Molecular Cloud are marked with a square; pre-stellar cores candidates are circled.

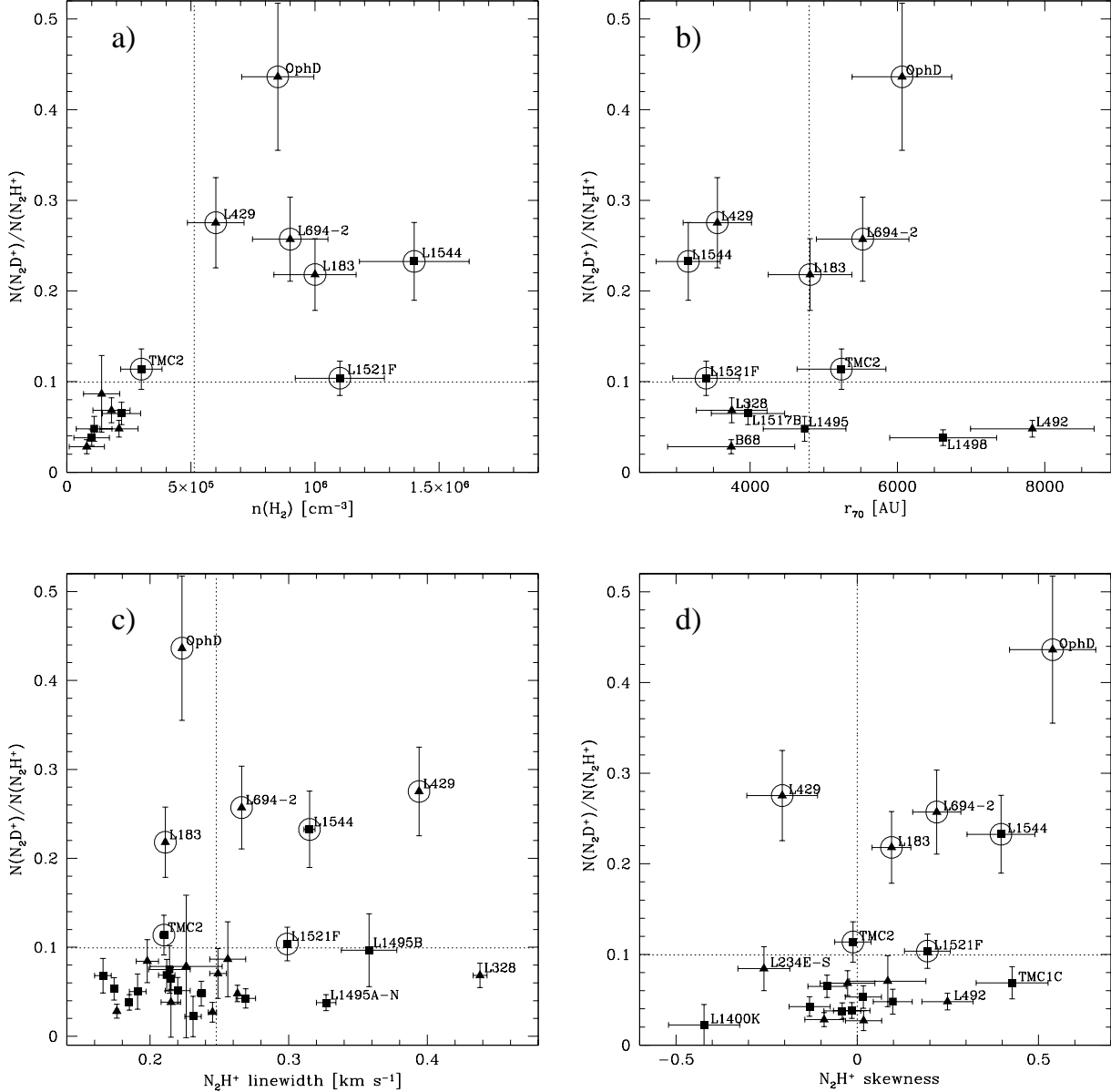


Fig. 6.— Deuterium fractionation correlations. In all panels: dotted lines are the arithmetic means of the distributions (but in panel d)); cores belonging to the Taurus Molecular Cloud are marked with a square; pre-stellar cores candidates are circled; the values were evaluated at  $\text{N}_2\text{D}^+$  peak position. **Panel a):** Deuterium fractionation vs.  $\text{H}_2$  central volume density. The  $n(\text{H}_2)$  values are taken from the literature (see Section 4.3), with the exception of TMC2, L492 and B68, estimated in this work. **Panel b):** Deuterium fractionation vs. equivalent radius of the flattened region  $r_{70}$  is defined as  $\sqrt{\text{area}_{70}/\pi}$ , with  $\text{area}_{70}$  as the area within the 70% contour in the 1.2-mm map. **Panel c):** Deuterium fractionation vs.  $\text{N}_2\text{H}^+(1-0)$  linewidth evaluated from the simultaneous fit of all the 7 hyperfine components. **Panel d):** Deuterium fractionation vs.  $\text{N}_2\text{H}^+(1-0)$  line asymmetry. The vertical dotted line separates the red-skewed spectra from the blue-skewed ones (the arithmetic mean is 0.07).

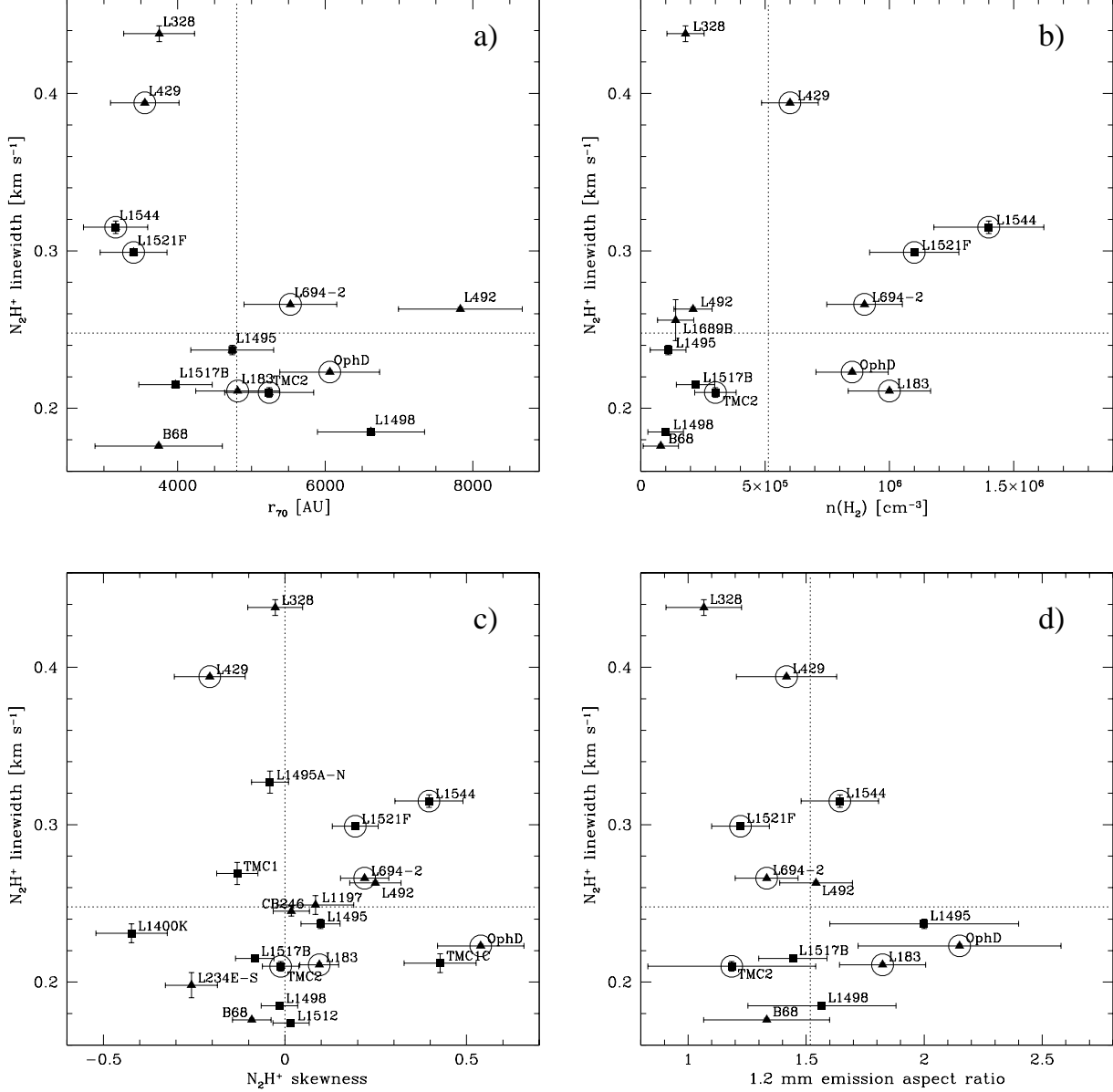


Fig. 7.— Correlations between “dynamical evolution” indicators. In all panels: dotted lines are the arithmetic means of the distributions (but in panel c)); cores belonging to the Taurus Molecular Cloud are marked with a square; pre-stellar cores candidates are circled; the values were evaluated at  $\text{N}_2\text{D}^+$  peak position. **Panel a):**  $\text{N}_2\text{H}^+(1-0)$  linewidth vs. equivalent radius of the flattened region  $r_{70}$  is defined as  $\sqrt{\text{area}_{70}/\pi}$ , with  $\text{area}_{70}$  as the area within the 70% contour in the 1.2-mm map. **Panel b):**  $\text{N}_2\text{H}^+(1-0)$  linewidth vs.  $\text{H}_2$  volume density. The  $n(\text{H}_2)$  values are taken from the literature (see Section 4.3), with the exception of TMC2, L492 and B68, estimated in this work. **Panel c):**  $\text{N}_2\text{H}^+(1-0)$  linewidth vs.  $\text{N}_2\text{H}^+(1-0)$  line asymmetry. The vertical dotted line here separates the red-skewed spectra from the blue-skewed ones (the arithmetic mean is 0.07). **Panel d):**  $\text{N}_2\text{H}^+(1-0)$  linewidth vs. aspect ratio of the 50% contour of the 1.2-mm emission.

Fig. 8.— L694-2 maps in 1.2-mm continuum, C<sup>18</sup>O(1–0), N<sub>2</sub>H<sup>+</sup>(1–0) and N<sub>2</sub>D<sup>+</sup>(2–1). N<sub>2</sub>H<sup>+</sup> and N<sub>2</sub>D<sup>+</sup> data were smoothed to a common resolution of 26'' and regridded; the reference position is the one reported in Table 1. The 1.2-mm map (Tafalla et al. in preparation) was smoothed to a resolution of 22''. Contour levels are 30% to 90% by 15% of the peak for each map. Peak values are 185 mJy/22'' beam for the 1.2-mm map and 5.16, 1.26 and 1.76 K km s<sup>−1</sup> for N<sub>2</sub>H<sup>+</sup>(1–0), N<sub>2</sub>D<sup>+</sup>(2–1) and C<sup>18</sup>O(1–0) respectively. Available 40''×40'' maps of N<sub>2</sub>H<sup>+</sup> and N<sub>2</sub>D<sup>+</sup>(3–2) are not reported because of poor S/N outside the peak.

Fig. 9.— L183 maps in 1.2-mm continuum, C<sup>18</sup>O(1–0), N<sub>2</sub>H<sup>+</sup>(1–0) and N<sub>2</sub>D<sup>+</sup>(2–1). Same as in Figure 8 but for the peak values: here 239 mJy/22'' beam for the 1.2-mm map and 4.31, 1.65, and 2.5 K km s<sup>−1</sup> for N<sub>2</sub>H<sup>+</sup>(1–0), N<sub>2</sub>D<sup>+</sup>(2–1) and C<sup>18</sup>O(1–0) respectively. The 1.2-mm map has been taken from Pagani et al. (2003). Available 30''×60'' maps of N<sub>2</sub>H<sup>+</sup> and N<sub>2</sub>D<sup>+</sup>(3–2) are not reported because of poor S/N outside the peak.

Fig. 10.— OphD maps in 1.2-mm continuum,  $N_2H^+(1-0)$  and  $(3-2)$  and  $N_2D^+(2-1)$  and  $(3-2)$ . Same as in Figure 8 but for the peak values: here 195 mJy/22" beam for the 1.2-mm map and 3.81, 0.49, 1.75 and 0.60 K km s<sup>-1</sup> for  $N_2H^+(1-0)$  and  $(3-2)$ ,  $N_2D^+(2-1)$  and  $(3-2)$  respectively. The 1.2-mm map has been taken from Ward-Thompson et al. (1999). The RMS of the  $N_2H^+(3-2)$  increase significantly towards north east, thus contours above -20" has to be taken with caution.

Fig. 11.— L429 maps in 1.2-mm continuum,  $N_2H^+(1-0)$  and  $(3-2)$  and  $N_2D^+(2-1)$  and  $(3-2)$ . Same as in Figure 8 but for the peak values: here 210 mJy/22" beam for the 1.2-mm map and 6.12, 0.63, 2.07 and 0.69 K km s<sup>-1</sup> for  $N_2H^+(1-0)$  and  $(3-2)$ ,  $N_2D^+(2-1)$  and  $(3-2)$  respectively. The 1.2-mm map has been taken from Bacmann et al. (2000).

Fig. 12.— L492 maps in 1.2-mm continuum,  $C^{18}O(1-0)$ ,  $N_2H^+(1-0)$  and  $N_2D^+(2-1)$ . Same as in Figure 8 but for the peak values: here 114 mJy/22" beam for the 1.2-mm map and 3.96, 0.31 and 1.69 K km s<sup>-1</sup> for  $N_2H^+(1-0)$ ,  $N_2D^+(2-1)$  and  $C^{18}O(1-0)$  respectively.

Fig. 13.— TMC2 maps in 1.2-mm emission smoothed to 22" (contour in both panels) and C<sup>18</sup>O(1–0) (greyscale in the upper panel) from new 30m observations and the N<sub>2</sub>H<sup>+</sup>(1–0) map (greyscale in the lower panel) taken by Caselli et al. (2002c) with FCRAO (HPBW 54" ; reference position here is the same as in Table 1). Contour levels starts from 30% of peak and increase by 15% of it. Peak values are: 138 mJy/22" beam for the 1.2-mm map, 2.12 K km s<sup>−1</sup> for the C<sup>18</sup>O observations. N<sub>2</sub>H<sup>+</sup>(1–0) intensity peak is 3.6 K km s<sup>−1</sup> in T<sub>MB</sub> temperature. In the bottom panel the positions of 7 young stars (in order of ascending RA: JH93, JH90, JH91, JH92, JH94 - Wendker 1995 ; FY Tau, FZ Tau - Nurmanova 1983) is reported with a five points star. Two IRAS point sources visible in the same field are reported with a filled square.

Fig. 14.— 1.2-mm continuum maps of 12 cores in our sample. Light contours are spaced from 10% to 90% by 10% of the peak; while the 98% and the 50% contours are represented with a bold line. The cross marks the mean position of the points within the 50% contour. The cores are ranked for increasing “cometariness”. This parameter is reported at the top right corner of each map and is calculated as the distance between the mean point and peak in units of r<sub>70</sub>. TMC2 and OphD were not included in this classification since they have multiple peaks within their 50% contour so this technique failed for them.

Fig. 15.— N<sub>2</sub>H<sup>+</sup>(1–0) velocity gradients towards the cores L694-2, OphD, L183, L429 and L492. The N<sub>2</sub>H<sup>+</sup>(1–0) data were regridded in a regular pattern. The integrated intensity maps are shown in greyscale (see Figures 8 - 12). Local velocity gradients in adjacent 9 points are represented with an arrow pointing in the direction of increasing velocity and with the length proportional to the magnitude (1 km s<sup>−1</sup> pc<sup>−1</sup> corresponds to a 6"-long arrow). Note that the angular scale of each map is the same.

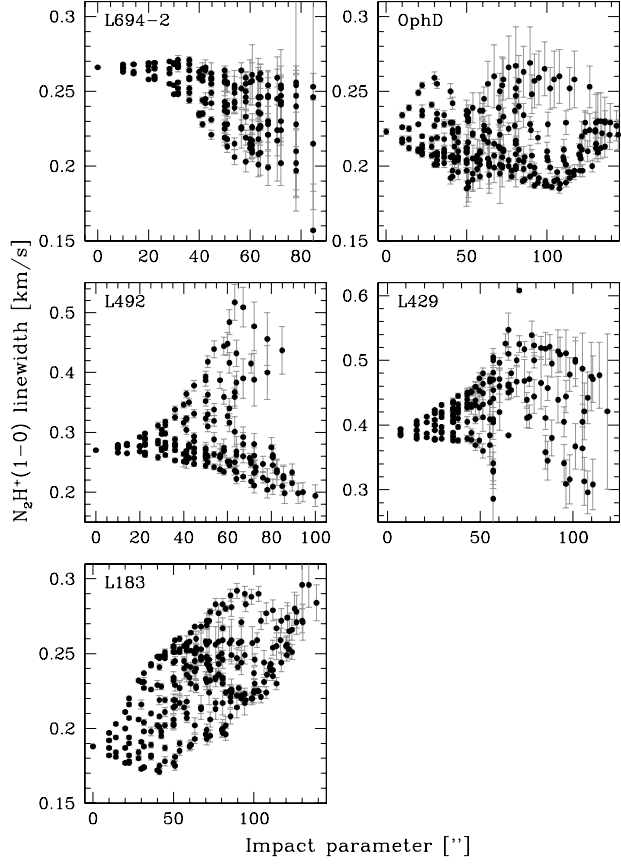


Fig. 16.—  $\text{N}_2\text{H}^+(1-0)$  intrinsic line width gradients within the cores L694-2, OphD, L183, L429 and L492. The angular offset was evaluated from the  $\text{N}_2\text{D}^+(2-1)$  peak position (see Table 3).

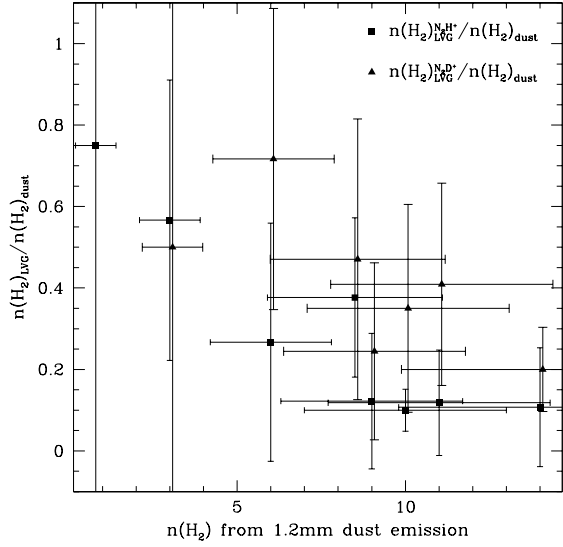


Fig. 17.—  $\text{H}_2$  central density derived from dust observation compared with the determination from  $\text{N}_2\text{H}^+/\text{N}_2\text{D}^+$  observations. The density inferred from the dust emission is always higher than the one derived from the molecular data, although the difference seem to diminish in the lowest density cores. Moreover, the estimates done starting from  $\text{N}_2\text{D}^+$  data furnish moderately higher  $\text{H}_2$  density, consistently with the idea that  $\text{N}_2\text{D}^+$  is a better tracer of the dust emission. Data points from  $\text{N}_2\text{D}^+$  were slightly offsetted in the x-axis in order to show them better.

This figure "f8.gif" is available in "gif" format from:

<http://arxiv.org/ps/astro-ph/0409529v1>

This figure "f9.gif" is available in "gif" format from:

<http://arxiv.org/ps/astro-ph/0409529v1>

This figure "f10.gif" is available in "gif" format from:

<http://arxiv.org/ps/astro-ph/0409529v1>

This figure "f11.gif" is available in "gif" format from:

<http://arxiv.org/ps/astro-ph/0409529v1>

This figure "f12.gif" is available in "gif" format from:

<http://arxiv.org/ps/astro-ph/0409529v1>

This figure "f13.gif" is available in "gif" format from:

<http://arxiv.org/ps/astro-ph/0409529v1>

This figure "f14.gif" is available in "gif" format from:

<http://arxiv.org/ps/astro-ph/0409529v1>

This figure "f15.gif" is available in "gif" format from:

<http://arxiv.org/ps/astro-ph/0409529v1>